The Upgraded CARISMA Magnetometer Array in the THEMIS Era

**I.R. Mann · D.K. Milling · I.J. Rae · L.G. Ozeke · A. Kale · Z.C. Kale · K.R. Murphy ·
A. Parent · M. Usanova · D.M. Pahud · E.-A. Lee · V. Amalraj · D.D. Wallis ·
V. Angelopoulos · K.-H. Glassmeier · C.T. Russell · H.-U. Auster · H.J. Singer**

Abstract This review describes the infrastructure and capabilities of the expanded and upgraded Canadian Array for Realtime InvestigationS of Magnetic Activity (CARISMA) magnetometer array in the era of the THEMIS mission. Formerly operated as the Canadian Auroral Network for the OPEN Program Unified Study (CANOPUS) magnetometer array until 2003, CARISMA capabilities have been extended with the deployment of additional fluxgate magnetometer stations (to a total of 28), the upgrading of the fluxgate magnetometer cadence to a standard data product of 1 sample/s (raw sampled 8 samples/s data stream available on request), and the deployment of a new network of 8 pairs of induction coils (100 samples per second). CARISMA data, GPS-timed and backed up at remote field stations, is collected using Very Small Aperture Terminal (VSAT) satellite internet in real-time providing a real-time monitor for magnetic activity on a continent-wide scale. Operating under the magnetic footprint of the THEMIS probes, data from 5 CARISMA stations at 29–30 samples/s also forms part of the formal THEMIS ground-based observatory (GBO) datastream. In addition to technical details, in this review we also outline some of the scientific capabilities of the CARISMA array for addressing all three of the scientific objectives of the THEMIS mission, namely: 1. Onset and evolution of the macroscale *substorm instability*,

I.R. Mann (✉) · D.K. Milling · I.J. Rae · L.G. Ozeke · A. Kale · Z.C. Kale · K.R. Murphy · A. Parent ·
M. Usanova · D.M. Pahud · E.-A. Lee · V. Amalraj
Dept. of Physics, University of Alberta, Edmonton, Alberta, Canada, T6G 2G7
e-mail: imann@phys.ualberta.ca

D.D. Wallis
Magnametrics, Ottawa, Ontario, Canada

V. Angelopoulos · C.T. Russell
Department of Earth and Space Sciences, University of California at Los Angeles, Los Angeles, USA

K.-H. Glassmeier · H.-U. Auster
Institut fur Geophysik und Extraterrestrische Physik, Technische Universitat Braunschweig,
Braunschweig, Germany

H.J. Singer
NOAA Space Weather Prediction Center, Boulder, CO, USA

2. Production of storm-time MeV electrons, and 3. Control of the solar wind-magnetosphere coupling by the bow shock, magnetosheath, and magnetopause. We further discuss some of the compelling questions related to these three THEMIS mission science objectives which can be addressed with CARISMA.

1 Introduction

The Canadian Array for Realtime InvestigationS of Magnetic Activity (CARISMA) magnetometer array is a network of ground-based magnetometers with stations deployed across the North American continent. The CARISMA array monitors the 3-D vector magnetic field and its fluctuations at the surface of the Earth, and hence can monitor the magnetic field perturbations driven in the magnetosphere by coupling to the solar wind. The global, meso-scale, and local magnetic effects from electrical current systems and waves can be remote-sensed using this network of sensitive instruments. These instruments monitor the magnetic perturbations arising from currents flowing in the magnetosphere, the magnetic plasma bubble carved out in the solar wind by the Earth's magnetic field, or in the ionosphere, a region of Earth's atmosphere above around 110 km altitude which is itself perturbed by currents and energetic particles from space. These magnetic perturbations provide the capability to remote-sense energy transfer and track disturbances driven in near-Earth space by the sun.

The CARISMA array operates as an integral part of the Canadian Geospace Monitoring (CGSM) program, a multi-instrument program funded by the Canadian Space Agency (CSA) whose goal is to "understand the transport of mass and energy across multiple scales throughout the solar-terrestrial system". CGSM has five grand challenge science themes, namely to address the processes that are responsible for:

- Driving magnetospheric convection and controlling energy injection into the global magnetosphere.
- The triggering and development of magnetotail instabilities and flows.
- The generation, modulation, and multi-scale structure of auroral arcs and auroral particle acceleration.
- The role of wave–particle interactions in the acceleration and loss of energetic particles in the magnetosphere.
- Cold plasma injection, transport, and loss in the global magnetosphere.

CARISMA data contributes to scientific examinations of the process and causes for all of these five CGSM grand challenge science themes.

Data from selected CARISMA stations also represent a formal element of the data set for the NASA Time History of Events and Macroscale Interactions during Substorms (THEMIS) mission (Sibeck and Angelopoulos 2008). CARISMA data will contribute directly to each of the science objectives of the THEMIS mission (see Angelopoulos 2008) which can be summarized as:

- Onset and evolution of the macroscale substorm instability.
- Production of storm-time MeV electrons.
- Control of the solar wind-magnetosphere coupling by the bow shock, magnetosheath, and magnetopause.

There are additional scientific foci for the CARISMA array within the framework of the CGSM grand challenge science themes, as well as support for the science objectives of the International Living with a Star (ILWS) program. However, in this paper we concentrate upon the THEMIS-related science capabilities of the CARISMA array.

In the following sections we describe the details of the CARISMA magnetometer array, including instrument characteristics and station locations, and then outline some of the key areas where the CARISMA magnetometer data will make a crucial contribution to reaching closure on the science objectives for the THEMIS mission. Section 3 briefly discusses the three THEMIS mission science objectives, and Sects. 4, 5 and 6 provide some case study examples and detailed discussion of CARISMA capabilities to address each objective. Section 7 then provides some conclusions.

2 The CARISMA Magnetometer Array

2.1 The Array

The CARISMA magnetometer array is the successor to the CANOPUS (Canadian Auroral Network for the OPEN Program Unified Study—see Rostoker et al. 1995 for details) magnetometer array. The CANOPUS magnetometer array operated as an integral part of the CANOPUS program, ran from 1986 to 2005, and made available magnetometer data from 13 stations at 5 s sampling resolution. The CARISMA project officially started on 1st April 2005, and data from CARISMA is available as a standard 1 s cadence data product and at the raw instrument sampling rate of 8 samples/s on request. CARISMA is operated by the University of Alberta as part of the CGSM program, and is funded by the CSA.

The thirteen original CANOPUS sites have undergone a program of upgrades to site infrastructure within the CSA CGSM program, supporting the continued real-time collection of scientific data from the magnetometers, riometers, meridian scanning photometers and all sky imagers deployed across the collective CGSM array. In the CANOPUS era the science instruments at each site were tightly coupled into a central processor, which built combined data packets for transmission over the Skyswitch satellite link. This has been replaced by autonomous science instrument data loggers which are linked to the internet via the Information Technology Infrastructure (ITI) firewall computer and associated hardware. The ITI provides a Ka-band satellite internet link, uninterruptible Power Supply (UPS), network switchable power outlets and GPS disciplined Network Time Protocol (NTP) timing for the science instruments. Each of the CGSM instrument arrays is operated under a separate contract from the CSA, and each instrument array has been developed further within CGSM under the leadership of the individual instrument array PI.

The CARISMA array now benefits from a significant upgrade as compared to the system which supported operation within the old CANOPUS magnetometer array. Most significantly, the new CARISMA magnetometer infrastructure addresses the most significant weakness of the previous system—the fact that there was no local data storage such that when the real-time satellite data transfer from the site to the central data archive was interrupted the data dropouts in fact represented a permanent loss of data. All CARISMA data is now stored at the remote site on the CARISMA data loggers' RAID disks, and data can be retrieved after any period of network downtime. An increase in bandwidth also allows the collection, retrieval and archiving of magnetometer data at the full 8 samples/s sampling rate, as compared to the previous CANOPUS array which could only provide a 5 second cadence data stream. GPS timing ensures that the CARISMA data time stamps have high
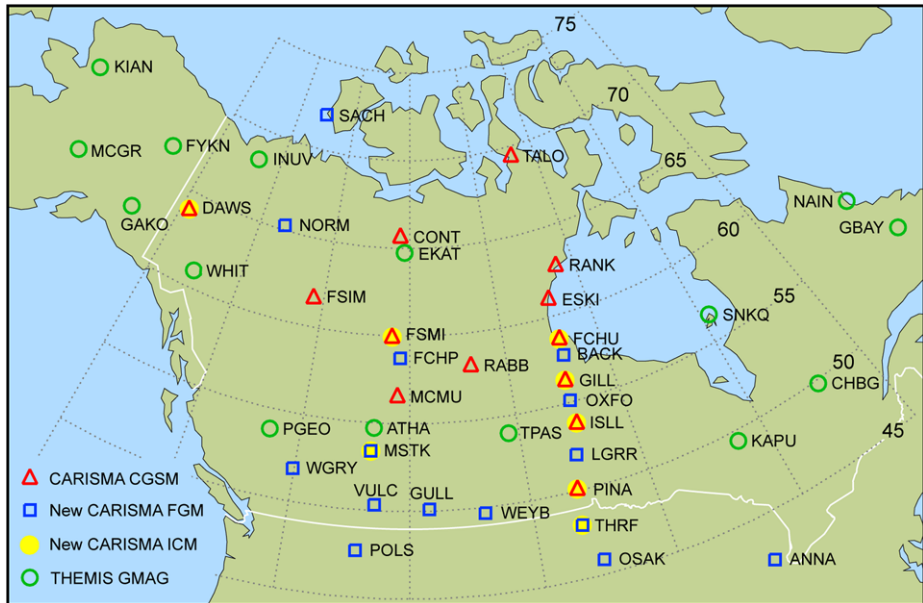
Fig. 1 The locations of the current CARISMA and THEMIS GMAG fluxgate magnetometers, together with the future CARISMA fluxgate (FGM) and search coil (SCM) magnetometers

accuracy, to within around 1 ms. Overall this creates an excellent high-quality data stream which is collected continuously from the CARISMA sites in near-real time over the Ka-band internet link.

The CARISMA network is also currently undergoing a significant expansion, funded by the Canadian Foundation for Innovation (CFI), with the deployment of 15 new fluxgate magnetometer sites underway and due to be finished by March 2009. With a total of 28 stations, CARISMA will constitute one of the foremost magnetometer arrays in the world. Additional stations will be added at strategic locations to improve the scientific capabilities of the array to: i) Provide coverage at mid-latitudes for plasmasphere, radiation belt, and sub-auroral polarization stream science; ii) Decrease Churchill line latitudinal spacing for cross-phase monitoring of the Alfvén continuum and total plasma mass density profiles; iii) Constitute a second meridional line in Alberta to enable some spatial (LT) and temporal (UT) ambiguities to be resolved, iv) Create a grid of stations at mid-latitudes enabling the location of the substorm current wedge (SCW), and Pi2, Pi1 and Pi1B timing, during substorm onset; and v) Provide additional coverage within the field of view of the western Canadian Super-DARN radars. Elements of the enhanced science capabilities afforded through operation of the new array are discussed further below.

In addition, induction coil magnetometers consisting of two crossed coils have been deployed at 8 of the expanded CARISMA array sites. The expanded array will be known as the CARISMA Magnetometer Network (CMN). The proposed CMN station locations are shown in Fig. 1. Site coordinates are given in Table 1.

The CMN covers over 25° in Geomagnetic Latitude (from $L \sim 2.8$ into the polar cap) and 5 hours in magnetic local time. The array is designed around 2 meridional chains, the Churchill line (333° magnetic longitude) and the Alberta line (308° magnetic longitude). These are connected by 2 chains at constant latitude, one in the auroral zone ($L \sim 6.6$) and

Table 1 CMN site coordinates CGM coordinates for 2008 at 100 km calculated using http://nssdc.gsfc.nasa.gov/space/cgm/cgm.html

Site code	Site name	Site type	Geodetic lat. (N)	Geodetic long. (E)	CGM lat. (N)	CGM long. (E)	L
CONT	Contwoyto	CGSM	65.75	248.75	72.9	304.6	11.7
DAWS	Dawson	CGSM	64.05	220.89	65.9	273.7	6.1
ESKI	Eskimo Point	CGSM	61.11	265.95	70.6	333.0	9.2
FCHU	Fort Churchill	CGSM	58.76	265.91	68.4	333.4	7.5
FSIM	Fort Simpson	CGSM	61.76	238.77	67.3	294.1	6.8
FSMI	Fort Smith	CGSM	60.03	248.07	67.3	306.7	6.8
GILL	Gillam	CGSM	56.38	265.36	66.1	332.9	6.2
ISLL	Island Lake	CGSM	53.86	265.34	63.7	333.2	5.2
MCMU	Fort McMurray	CGSM	56.66	248.79	64.2	309.0	5.4
PINA	Pinawa	CGSM	50.20	263.96	60.0	331.6	4.1
RABB	Rabbit lake	CGSM	58.22	256.32	66.9	319.0	6.6
RANK	Rankin Inlet	CGSM	62.82	267.89	72.3	335.8	11.0
SACH	Sachs Harbour	CGSM	71.99	234.74	76.2	280.0	NA
TALO	Taloyoak	CGSM	69.54	266.45	78.4	330.7	NA
BACK	Back	CFI	57.72	265.83	67.4	333.4	6.9
WGRY	Wells Gray	CFI	51.88	239.97	57.8	299.8	3.6
VULC	Vulcan	CFI	50.37	247.02	57.7	308.7	3.6
FCHP	Fort Chipewyan	CFI	58.77	248.89	66.3	308.4	6.3
GULL	Gull Lake	CFI	50.06	251.74	58.2	314.8	3.7
LGRR	Little Grand Rapids	CFI	52.03	264.54	61.9	332.3	4.6
MSTK	Ministik Lake	CFI	53.35	247.03	60.7	307.9	4.2
NORM	Norman Wells	CFI	65.26	233.31	69.6	285.5	8.3
POLS	Polson	CFI	47.66	245.79	54.7	307.9	3.1
OSAK	Osakis	CFI	45.87	264.92	55.9	333.4	3.2
OXFO	Oxford House	CFI	54.96	264.47	64.7	331.8	5.6
THRF	Thief River Falls	CFI	48.03	263.64	57.9	331.4	3.6
WEYB	Weyburn	CFI	49.69	256.20	58.6	320.8	3.7
ANNA	Ann Arbor	CFI	42.42	276.10	53.0	349.4	2.8

the other at mid-magnetic latitudes ($L \sim 3.6$). A small number of other sites are deployed to extend the coverage in both latitude and longitude. The highest concentration of sites will be deployed along the Churchill line to increase the latitudinal spatial resolution to a density where the average station separation is ~ 170 km. This is designed to be particularly useful for density diagnosis by the cross-phase technique (discussed further below). The inter-station separation is less dense along the Alberta line but will still yield very useful information for resolving UT/LT spatio-temporal ambiguities. The majority of the new stations have been added at mid-latitudes which will enable the array to be used for substorm location studies, for instance using the substorm current wedge modeling technique described in Sect. 3.1, or for substorm timing with waves in the Pi2 or Pi1 bands (e.g. Jacobs et al. 1964). The additional station coverage will also provide the capability to monitor the dynamics and erosion of the plasmapause and plasmasphere, using the cross phase technique, as well as the characteristics of ultra-low frequency (ULF) waves which propagate

or are excited in the mid-latitude magnetosphere in the region magnetically conjugate to the outer Van Allen radiation belt.

2.2 Instrumentation

2.2.1 Fluxgate Magnetometers

The ringcore fluxgate magnetometers used in the CANOPUS array were designed and built by Narod Geophysics Ltd (NGL). They continue to operate reliably and have yielded high quality data since 1989. An upgraded version of this design has been supplied by NGL for the expansion of the CARISMA array. The instruments are very similar except where end-of-line electronic components needed to be replaced. The specifications of the fluxgate magnetometers are given in Table 2.

Note that the noise level of the new instrument has actually increased slightly as compared to the earlier CANOPUS instruments due to the lack of availability of the previous generation's ringcore material. However, the noise floor is still less than the amplitude resolution of the instrument and so in practice the performance of the instruments remains high and comparable to that obtained in the previous generation.

2.2.2 Induction-Coil Magnetometers

The induction-coil magnetometers (also known as search coil magnetometers) deployed in the expanded CARISMA array are LEMI-30 sensors designed and built by the Lviv Centre of Institute of Space Research, Ukraine. The specifications are given in Table 3.

Table 2 NGL magnetometer specifications

Characteristic	Specification
Dynamic range	± 70000 nT
Resolution	0.025 nT
Temperature stability	<0.1 nT/°C
Drift	<0.01 nT/day
RMS noise	S100: <7 pT/$\sqrt{}$Hz at 1 Hz
	CFI: <20 pT/$\sqrt{}$Hz at 1 Hz
Sampling rate	8 Hz
Low-pass cutoff	2 Hz
Power	<1.3 W average

Table 3 Induction coil magnetometer specifications

Bandwidth	0.01 to 30 Hz	
Sensitivity	Channel 1:	Channel 2:
	20 mV/nT (1 to 30 Hz)	200 mV/nT (1 to 30 Hz)
	20 * f mV/nT (0.01 to 1 Hz)	200 * f mV/nT (0.01 to 1 Hz)
Sensitivity error	<3 dB	
Magnetic noise level	<0.2 pT/$\sqrt{}$Hz @ 1 Hz	
Noise rejection	>60 dB at 60 Hz	
Operating temperature range	-10 to $+50$°C	

2.3 Data Products and Data Access

The CARISMA data is distributed by the Canadian Space Science Data Portal (CSSDP) via the website http://www.cssdp.ca. The raw 8 sample/s data is filtered and decimated to yield 1 sample/s day-files which are the primary data product available on the CSSDP. The CSSDP functionality also allows the browsing of summary plots and provides an interface to a user-defined plotting tool which allows time ranges and filtering to be applied to data which is retrieved and displayed in plots within CSSDP. The full 8 samples/s resolution data is available on request to the CARISMA PI.

An additional data product is also produced at 2 samples/s cadence from five of the CARISMA sites at Fort Simpson, Fort Smith, Rankin Inlet, Gillam, and Pinawa. To form this data set, the data is decimated to 2 samples/s and rotated from the measured geographic coordinate system into local geomagnetic coordinates. This data stream is provided on a next day basis to the THEMIS Science Operations Center (SOC) at the University of California, Berkeley. This 2 samples/s CARISMA data forms an integral and formal element of the THEMIS Ground-Based Observatory (GBO; see also Mende et al. 2008) magnetometer data set, as per a NASA-CSA formal letter of agreement. Provision of the remaining CARISMA data in a 2 samples/s data product is also planned. The search-coil magnetometer data will be made routinely available at 20 samples/s (and on request at 100 samples/s) resolution, and in addition we will publish daily dynamic spectrograms from each site.

The CARISMA team are also founding members of the Ultra Large Terrestrial Magnetometer Array (ULTIMA; http://www.serc.kyushu-u.ac.jp/ultima/ultima.html) a collaboration and formal partnership between operators of international magnetometer networks, promoting scientific cooperation, collaboration, and mutual exchange of scientific data from world-wide arrays.

3 THEMIS Science with CARISMA

The upgraded and expanded CARISMA array can provide data which represents a crucial contribution toward science closure on the three THEMIS mission science objectives. The GBO network which forms part of the THEMIS mission provides global scale instrument coverage in the North American sector, both optically and magnetically. In the prime mission phase, the THEMIS orbits are designed to make repeated magnetic conjunctions to the Canadian sector. The ground-based data from the GBOs and from additional programs such as CARISMA provides an unprecedented framework in which to interpret the scientific data from the five THEMIS probes. In the following subsections, we briefly outline some of the scientific capabilities of the CARISMA array in the context of the three THEMIS science objectives. In Sects. 4, 5 and 6 we illustrate the CARISMA array capabilities with scientific examples from the THEMIS mission thus far.

3.1 Onset and Evolution of the Macroscale Substorm Instability

One of the most important outstanding questions in Space Physics concerns understanding the explosive dynamics of the magnetotail during substorm expansion phase onset. The location of, and relative timing between, the physical processes which constitute the substorm expansion phase remain controversial. The onset of the expansion phase of the magnetospheric substorm is marked by a rapid topological change in the magnetic field configuration in the nightside magnetosphere, resulting in a rapid transfer of energy from

the magnetotail into the ionosphere, and triggering vibrant and dynamic auroral displays. There are two competing models proposed to explain substorm onset. Both models agree on the importance of magnetic reconnection at a near-Earth neutral line (NENL) at around 20–25 R_E to power the substorm, but disagree on the causal sequence of events. In the so-called current disruption model, onset initiates closer to the Earth (around 10–15 R_E) and is followed later by NENL reconnection once disturbances from the near-Earth onset reach the mid-tail. In the NENL model, it is reconnection at the NENL which begins the expansion phase and nearer-Earth disturbances follow (see e.g. Lui et al. 1991; Angelopoulos 2008).

The study of the "onset and evolution of the macroscale substorm instability" is the primary objective of the THEMIS mission. Specifically, the THEMIS mission targeted measurements to address the following topics:

- Establish when and where substorms start.
- Determine how the individual substorm components interact macroscopically.
- Determine how substorms power the aurora.
- Identify how the substorm instability couples dynamically to local current disruption modes.

The coverage from the ground arrays, including CARISMA, is key to tackling these problems. Especially important is the need to establish the location of the THEMIS probes in the context of the ionospheric auroral and magnetic signatures of the substorm onset process(es). Despite uncertainties in the mapping from the ionosphere to the near-Earth tail, the ground-based context of the disturbances and the sequence of events leading to the in-situ perturbations measured by the probes is crucial if the causality and time sequence of events are to be correctly identified. In Sect. 4 below, we illustrate how CARISMA and supporting magnetometer network data can be used to constrain the substorm process. We concentrate on a case study example from the 7th March 2007. This event followed the launch of the THEMIS probes on February 17th 2007, but was sufficiently early in the commissioning phase that only the fluxgate magnetometers (FGM; see Auster et al. 2008) were operating following the magnetometer boom deployment on all probes.

3.2 Control of the Solar Wind–Magnetosphere Coupling by the Bow Shock, Magnetosheath, and Magnetopause

The orbit of the THEMIS probes generates a configuration whereby the apogees of the probes align over the Canadian continent in their prime science phase configuration. This allows the constellation to sample regions of the upstream solar wind, the bow shock region, magnetosheath, magnetopause and even inside the magnetosphere, at the same time producing the unique capability to monitor the energy flow and processing of upstream solar wind disturbances by the bow shock and magnetopause boundaries. As with the substorm studies described in Sect. 3.1 above, the continent-scale ground-based magnetic monitoring provided by CARISMA has the capability to diagnose the magnetic signatures of this coupling on the ground. Scientific targets which can be addressed include the waves, current systems and convection driven by (see also Angelopoulos 2008):

- Pc3–4 upstream waves and IMF conditions (e.g. Le and Russell 1996);
- Sudden Impulses (SI$^{+/-}$ e.g. Araki 1994; Takeuchi et al. 2000);
- Traveling Convection Vortices (TCVs; e.g. Glassmeier 1992; Kivelson and Southwood 1991; Kataoka et al. 2003; Murr and Hughes 2003);
- Hot Flow Anomalies (HFAs; e.g. Sibeck et al. 1999);

- Fast solar wind streams and magnetopause Kelvin-Helmholtz instability (e.g. McKenzie 1970; Pu and Kivelson 1983; Miura 1992; Mann et al. 1999; Fairfield et al. 2007, and references therein);
- Solar wind dynamic pressure fluctuations (e.g. Kepko et al. 2002; Mathie and Mann 2000c);

In this review we concentrate including the effects of solar wind pressure pulses and KH shear flow instabilities excited at the magnetopause, and these are outlined in Sect. 5.

3.3 Production of Storm-Time MeV Electrons

One of the most interesting and important questions in current solar-terrestrial physics research concerns the acceleration of electrons to relativistic speeds in the Earth's Van Allen radiation belts. The fundamental mechanisms proposed to explain the dynamics, energization and loss of these particles are numerous, and which processes are dominant in response to different solar wind forcing conditions remains largely unknown (see e.g. the review by Friedel et al. 2002). Likely the most influential acceleration mechanisms are resonance with VLF lower band chorus, which operates through violation of the first adiabatic invariant (e.g. Meredith et al. 2003; Chen et al. 2007, and resonance with ULF waves which typically operates through violation of the third (e.g. Fälthammer 1966; Schulz and Lanzerotti 1974; Elkington et al. 2002). CARISMA has an excellent capability for studies of ULF wave related radiation belt acceleration and loss processes, including the drift resonant interaction with ULF waves as well as studies of the potential role of electromagnetic ion cyclotron (EMIC) waves for scattering MeV energy electrons into the loss cone and hence into the atmosphere (e.g., Horne and Thorne 1998; Friedel et al. 2002; Meredith et al. 2003; Summers and Thorne 2003).

A very surprising recent observation is the correlation of the inner edge of the radiation belt with the plasmapause (e.g. Tverskaya et al. 1986; O'Brien and Moldwin 2003; Li et al. 2006). One suggestion links this to the operation of VLF acceleration just outside the plasmasphere, with internal loss such as that occurring due to resonance with plasmaspheric hiss scattering the radiation belt particles internal to the plasmasphere into the atmosphere (e.g. Meredith et al. 2007). Alternatively, if a large element of radiation belt morphology is determined by inwards (and outwards; e.g. Shprits et al. 2004, 2005) diffusion then perhaps the effects of plasma density in controlling the penetration of ULF wave power to low-L such as that described by Loto'aniu et al. (2006) plays an important role. Comparing CARISMA observed ULF power, and energetic particle flux measured in-situ on-board THEMIS (with the solid state telescope (SST) for energies up to 900 keV) and other satellites, allows the role of ULF waves in producing the observed correlation to be tested.

Since plasma density can also influence the growth rates of EMIC waves (e.g. Kozyra et al. 1984), and therefore the efficiency of EMIC scattering of MeV electrons into the loss cone (e.g. Meredith et al. 2003), the plasmasphere and plasmapause morphology and location can be expected to influence radiation belt loss. A powerful remote-sensing capability of the CARISMA array involves the use of the properties of the waves supported by the plasma to determine the natural standing Alfvén wave eigenfrequencies of entire closed field lines. Through the solution of this inversion problem, the mass density in the equatorial plane can be determined in an assumed magnetic field. This so-called "cross-phase" technique (e.g. Baransky et al. 1985; Waters et al. 1991, 1995, 2002; Menk et al. 2000; Dent et al. 2003, 2006) enables the CARISMA array to monitor the equatorial mass density of field lines conjugate to CARISMA stations. This capability delivers a powerful means of studying the

structure of plasmasphere itself, as well as supporting studies of the influence of mass density on radiation belt dynamics. Examples illustrating the use of CARISMA data in support of radiation belt studies are presented in Sect. 6.

4 Substorm Science Capabilities

In the following subsections, we detail the analysis that can be performed with ground magnetometry to examine the characteristics of the processes and causal sequence of events associated with substorm onset. We utilize an early cruise-phase "THEMIS substorm" on the 7th March 2007 to present a case study which illustrates the science capabilities of the CARISMA array in support of substorm science. There were three substorms during the period 03-09 UT on the 7th March 2007 and we study the second substorm during this interval whose onset occurred at ∼0600 UT, where the CARISMA "Churchill Line" was situated close to magnetic midnight. During the period 0300-0700 UT, the ionospheric footprint of the THEMIS constellation first mapped to the Canadian sector and then towards the end of the interval to the Alaskan sector. The GOES geosynchronous spacecraft also provide a valuable in-situ resource for substorm studies, the CARISMA magnetometer array being particularly well-suited since GOES East (GOES-12 at this epoch) and GOES west (GOES-11 at this epoch) span the range of longitudes covered by the ∼geosynchronous chain of CARISMA magnetometers (DAWS-FSIM-FSMI-RABB-GILL). In addition to THEMIS magnetic conjunctions, the GOES satellites provide the capability for contemporaneous ground-spacecraft conjugate studies of geophysical phenomena on the same flux tube including an examination of substorm depolarization and studies of onset related Pi2 waves (see e.g., the review by Olson 1999), the highest resolution GOES magnetic field data (0.512 s resolution) also allowing studies of higher frequency Pi1 (cf. Lessard et al. 2006) and EMIC waves.

4.1 In-situ THEMIS and GOES Measurements

During this substorm the THEMIS probes were in the cruise-phase whereby their orbits were constrained to a "string-of-pearls" configuration. On the 7th March 2007, the CARISMA ground magnetometers were hence not directly magnetically conjugate to the THEMIS probes during the substorm onset at ∼06 UT. The THEMIS probes were separated from the CARISMA Churchill line (330° magnetic meridian) by ∼2 hours of local time at 08 UT and by the end of this period at 08 UT were ∼5 hours to the west. During this time the THEMIS probes were out-bound around the dusk flank.

Figure 2 shows the THEMIS FGM data for the interval 0500-0700 UT. The THEMIS spacecraft are traversing the dusk-side magnetosphere close to apogee at radial distances between ∼11–14 R_E during this interval. From top to bottom, Fig. 2 shows FGM data from TH-A, TH-B, TH-C, TH-D and TH-E in the GSM x (blue), y (green) and z (red) directions. There is a small dipolarization evident in B_z in 3 of the 5 spacecraft around 0545 UT, which is curiously not observed in TH-C and TH-E, and a B_y variation around the same time observed in all 5 spacecraft, perhaps indicative of nightside depolarization on the flanks. Note that there is also a dipolarization and associated B_y perturbation around 0610 UT.

In this interval, the ionospheric footprint of GOES-11 is situated close to FSIM, and the ionospheric footprint of GOES-12 is less than an hour of local time to the east of GILL, close to the CANMOS magnetometer and THEMIS ASI site at SNKQ. Figure 3 shows the high-resolution (0.512 s) GOES-11 (west) and -12 (east) magnetic field data in local field-aligned coordinates for the interval 0500-0700 UT. In the co-ordinate system used here p is
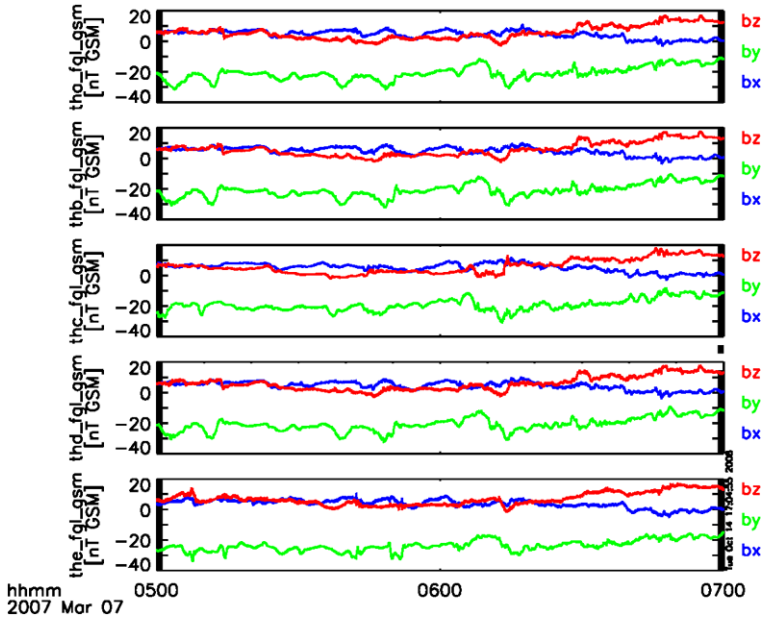
Fig. 2 Fluxgate magnetometer data from the THEMIS probes (A to E in the *top* to *bottom* panels, respectively) in GSM co-ordinates from 0500-0700 UT on the 7th March 2007
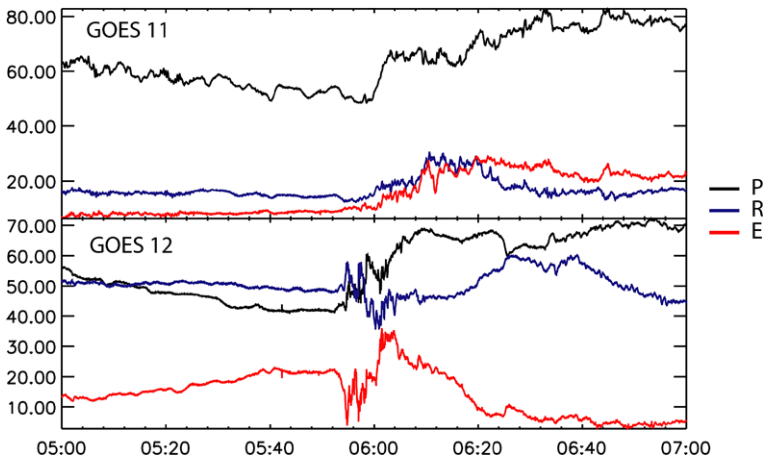

Fig. 3 GOES-11 and -12 magnetic field data from 0500-0700 UT on 7th March 2007 in p, r, and e coordinates (for details see text)

northward and perpendicular to the satellite orbit (parallel to the Earth's spin axis in a 0° inclination orbit, e is perpendicular to p and is directed earthward and is hence approximately radial, and n completes the triad, is directed eastward and is approximately azimuthal. Clear from Fig. 3 is the dipolarization in Hp, evident in both spacecraft at around ~0559 UT and ~0554 UT for GOES-11 and -12, respectively. In general, in order to interpret in-situ point

measurements such as these, the broader continent scale monitoring provided by CARISMA as well as the THEMIS GBOs is crucial.

4.2 Substorm Timing and Location with CARISMA

4.2.1 Substorm Bays

Figure 4 shows the (Fig. 4a) H- and (Fig. 4b) D-component ground magnetograms from the Canadian sector from the CARISMA and THEMIS GMAG arrays for the same interval 0500-0700 UT. Figure 4 is arranged in latitude and longitude order such that the magnetic traces at the top (bottom) of the figures are the most eastern (western) stations. Clear in Fig. 4a is the presence of a substorm, identified as a large bay, for example, in the FCHU-GILL traces at ∼0550 UT. The bays develop in response to the substorm current wedge (SCW) which is believed to be established through a diversion of the cross tail magnetospheric current into the ionosphere (e.g. McPherron et al. 1973). In this model, a downward field-aligned current (FAC) is established to the east, closes along the electrojet latitude in the ionosphere, and returns to connect to the cross tail current in a upward FAC which flows back to the tail to complete the circuit known as the SCW.

The magnitude and sign of the magnetic bays which develop at stations deployed across a latitudinal and longitudinal grid depends on the location of the stations with respect to the SCW and each of the H, D and Z components on the ground are affected (Cramoysan et al. 1995; Smith et al. 1999). We discuss this further below. At auroral latitudes, the Alfvén waves which must propagate to establish the SCW FAC elements are believed to bounce between the plasmasheet and the ionosphere, multiple reflections creating the Pi2 pulsations which "ride" on the back of the SCW bays as the FAC elements are established.

4.2.2 Substorm Pi2 Waves

A traditional method for timing substorm onset is to filter the ground magnetic perturbations in the Pi2 (40–150 s period) band. Figure 5 shows the Pi2 filtered H-component magnetometer data, together with similarly Pi2 filtered GOES-11 and GOES-12 p-component magnetometer data. Clear in Fig. 5 is that stations poleward of the electrojet (e.g., RANK) observe the Pi2 onset at later times than those closer to the onset latitude (e.g., TPAS). Using the Pi2 pulsations in Fig. 5, we can coarsely estimate substorm onset to be ∼0554 UT. However, since the Pi2 pulsation has a period of ∼2 minutes, it is virtually impossible to calculate the time at which the signal rises out of the noise to within a time accuracy that is shorter than the period of the wave. By looking at shorter period ULF waves and using improved time series analysis techniques, this uncertainty can be improved.

4.2.3 Substorm Pi1 Waves

Figure 6 shows the Pi1 (1–40 s) filtered H-component magnetometer data for the same stations and time period, together with similarly filtered GOES-11 and GOES-12 p-component data. In Fig. 6, the Pi1 signal rises out of the noise clearly at an earlier time than is obvious in Fig. 5, the most obvious onsets being at GILL, ISLL, PINA and MSTK prior to 0554 UT. Also notable in Fig. 6 is that there appears to be a pattern in the onset times of the Pi1 pulsations from station to station depending on their relative locations. For example, the onset of the large amplitude band-pass filtered Pi1 pulsations appears to be around 0554 UT at TPAS, but similar large amplitude Pi1 wavepackets only appear at a much later time shortly
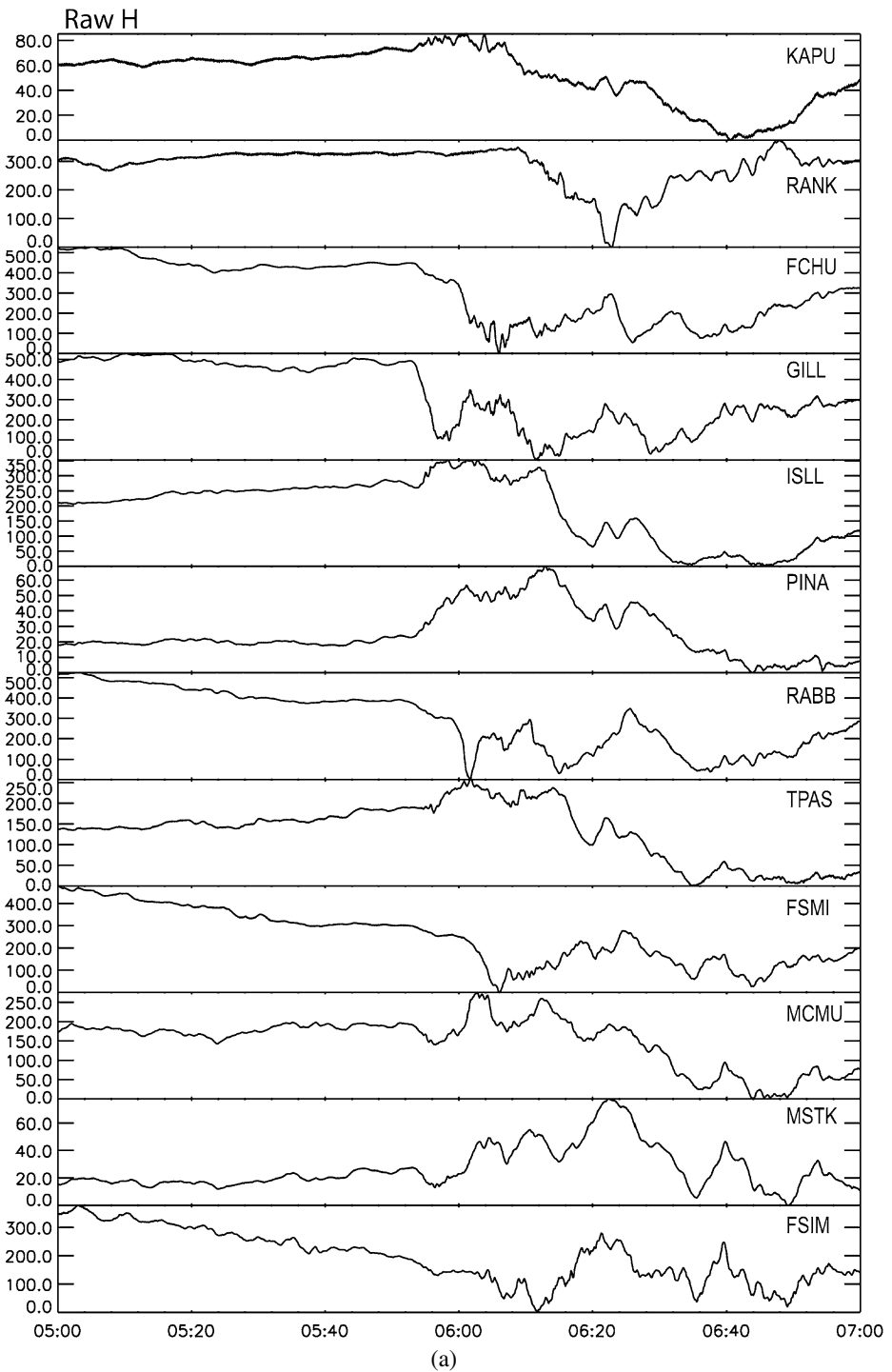
Fig. 4a Selected CARISMA, THEMIS and CANMOS H-component magnetometers from 0500-0700 UT on the 7th March 2007
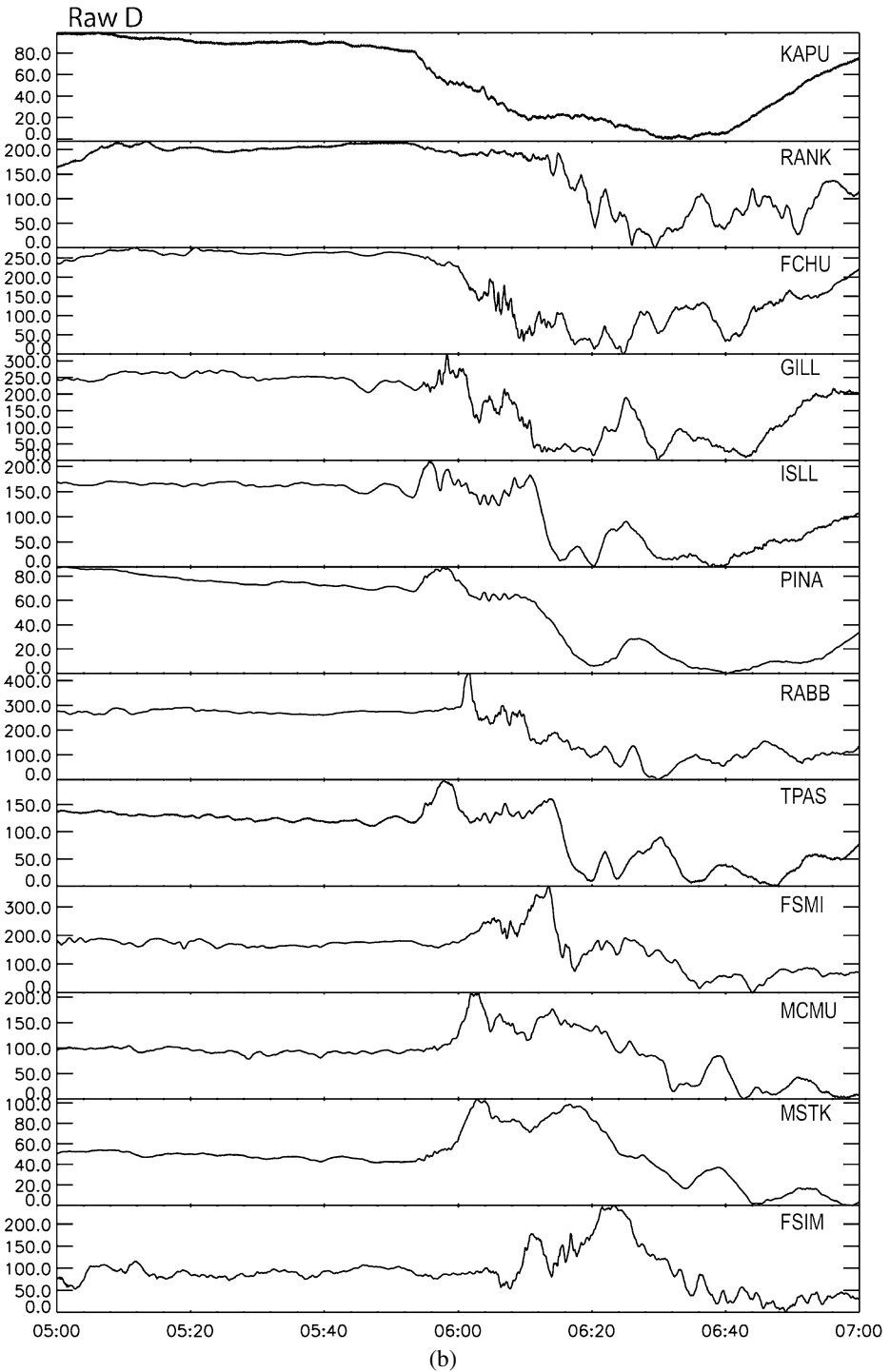
Fig. 4b Selected CARISMA, THEMIS and CANMOS D-component magnetometers from 0500-0700 UT on the 7th March 2007
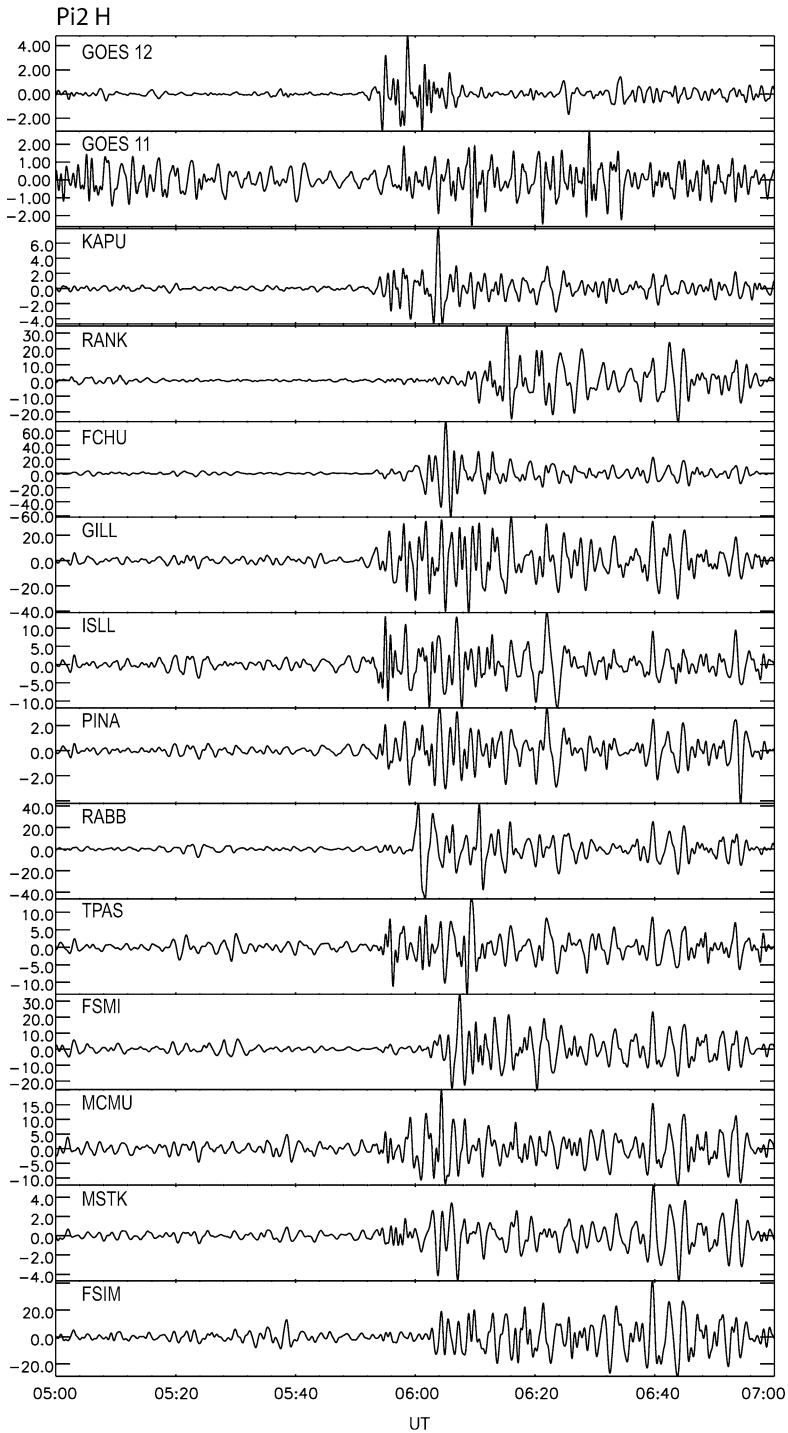
Fig. 5 Selected CARISMA, THEMIS and CANMOS Pi2 filtered (40–200 s) H-component magnetometers from 0500-0700 UT on the 7th March 2007
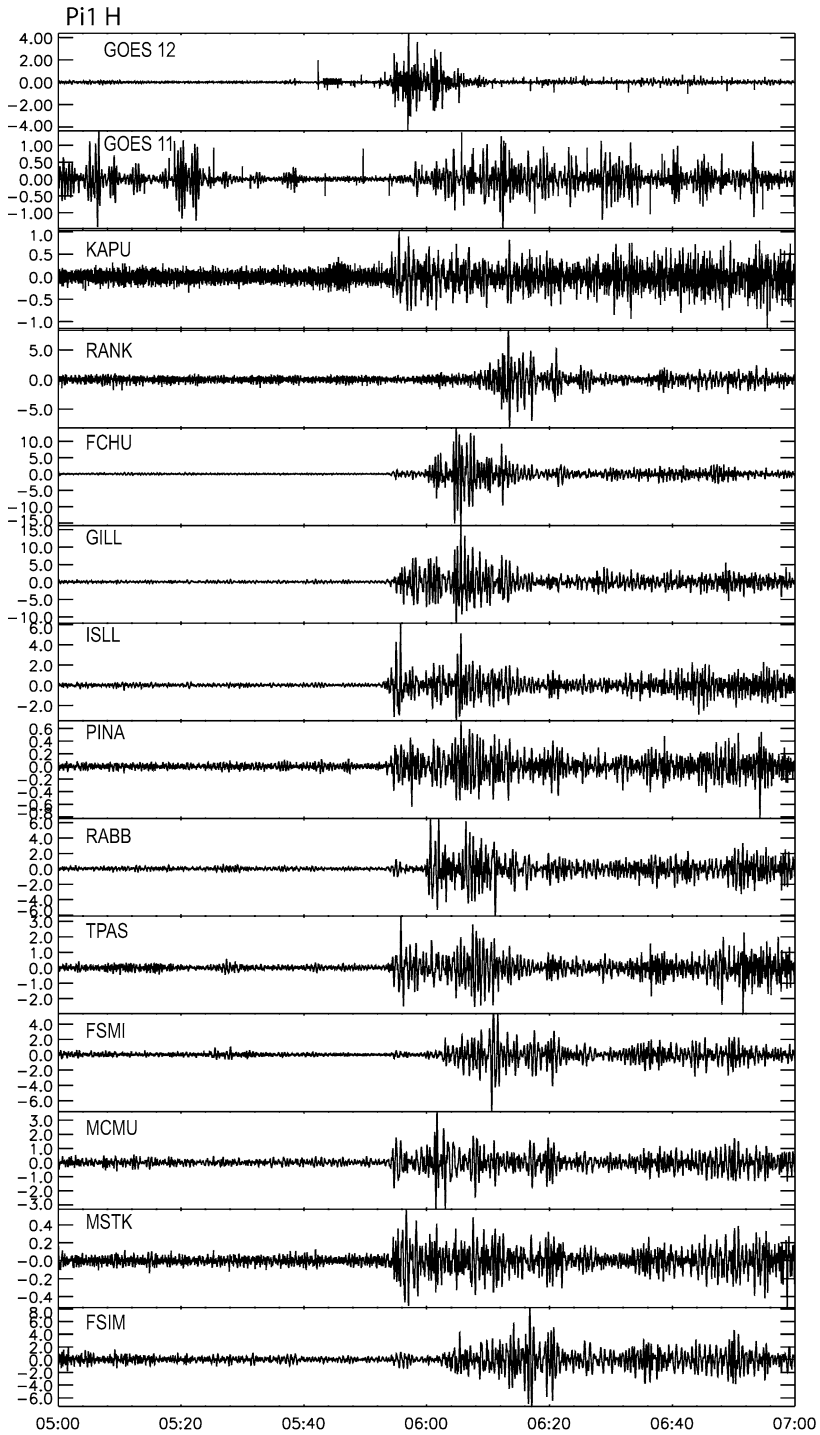
Fig. 6 Selected CARISMA, THEMIS and CANMOS Pi1 filtered (1–40 s) D-component magnetometers from 0500-0700 UT on the 7th March 2007

after 0600 UT at RABB, and even later (∼0602 UT) at FSMI. Figure 6 illustrates an element which requires caution when using filtered time-series to identify pulsation onset times and propagation. Even though the largest amplitude Pi1 wavepackets appear to be delayed from, for example, TPAS to RABB and FSMI, there is a much smaller amplitude wavepacket which appears earlier at FSMI, and especially clearly at FSIM and RABB, which is more contemporaneous with the TPAS magnetic Pi1 onset. Similar features were seen for example in the study of Arnoldy et al. (1998) in relation to Pi1B waves, these authors suggesting the large amplitude Pi1B propagation polewards from a mid-latitude onset region followed the poleward motion of the optical auroral surge at substorm onset, whilst the lower amplitude more contemporaneous Pi1B wave propagation might be linked to ionospheric ducting. Using more advanced wavelet time-series analysis techniques, we can use formal definitions of threshold powers to definitively determine the timing of the onset of the ULF pulsations, and Pi1 pulsations in particular. We can therefore mathematically determine propagation delays across the array by using the time at which the signal rises above the preceding noise, providing a systematic timing which improves upon the estimates that are currently often obtained by eye.

4.2.4 Wavelet Substorm Onset Timing and Location

The Discrete Wavelet Transform (DWT) is a method to decompose a time series into basis functions (wavelets) that are localized in both frequency and time. In this study, we utilize the Meyer wavelet outlined and applied to the Pi2 waveform by Nose et al. (1998). The Meyer wavelet is band-limited in frequency, and therefore minimizes overlap between adjacent wavelet bins. Wavelet coefficients with large J have a high time resolution but a low frequency resolution and vice versa. An important aspect of the Meyer wavelet is the resemblance of the waveform to an impulsive ULF wave such as the Pi1 and Pi2. Table 4 shows the frequency range and time resolution of the Meyer wavelet coefficients for a time series of 512 points. For details of the analysis techniques and detailed analysis of an isolated substorm, we refer the reader to Milling et al. (2008) and to Murphy et al. (2008) and Rae et al. (2008a, 2008b) for further details of the technique.

The DWT enables the waves in both the Pi1 and Pi2 bands to be analyzed at the same time using different wavelet coefficients, J. An onset time for each station for each J can be determined by first finding a quiet period and performing the DWT on this data. The mean and standard deviation are then determined for each J. The onset for any coefficient

Table 4 Frequency and time resolution for the Meyer wavelet functions on the 512-point time series used in this study

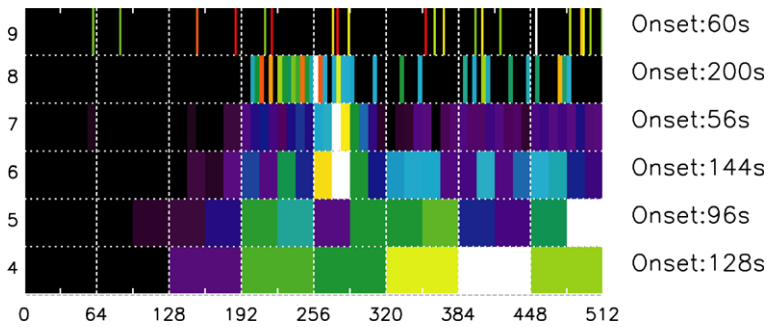| Band J	Frequency range (mHz)		Period range (seconds)		Resolution (seconds)
9	166.67	666.67	1.5	6	2
8	83.33	333.33	3	12	4
7	41.67	166.67	6	24	8
6	20.83	83.33	12	48	16
5	10.42	41.67	24	96	32
4	5.21	20.83	48	192	64
3	2.60	10.42	96	384	128
2	1.30	5.21	192	768	256

Fig. 7 (Colour online) Meyer DWT analysis of the SNKQ ground magnetometer station. The *y*-axis represents the power in different wavelet *J* bands (higher *J* represents higher frequency), and the *x*-axis denotes seconds since 0550 UT. Colour represents normalized DWT coefficient power, where *blue* is low power, and *yellow-red* is high DWT coefficient power. The onset times listed represent the first time that power in that particular *J* band rises above a threshold of two standard deviations from the mean defined in terms of earlier noise, indicating a change in the characteristics of the power at that time (see text for details)

J is then the initial time when the power in that coefficient rises above the mean plus two standard deviations of the power during the quiet period. Using the technique outlined above for the determination of a noise threshold means that there is a 98% chance that the signal observed is not noise of the same kind as observed during the preceding interval. The onset time for a given magnetometer station is then defined as the earliest onset time from all frequency bands, *J*. The power in any *J* band is calculated using the vector sum of the power from the H- and D-components such that we estimate the time when any transverse perturbation in the same frequency band rises above the defined threshold.

Figure 7 shows the results of the Meyer DWT analysis outlined above on the SNKQ magnetometer data, and starting from epoch time zero at 0551 UT. Figure 7 is a plot of the power in particular *J* bands. Since each *J* wavelet has a different length in the time series, dependent on the frequency being analyzed, the temporal resolution changes for each *J*. The power is colour coded such that purple/blue is low power, and white is the highest power, normalized to each frequency band. For example, only two wavelet coefficients are needed to describe character of the *J* = 2 band in a 512 point time series, each coefficient representing 256 points from that time series. For the *J* = 9 frequency band, 256 coefficients are required, which in this particular time series (1 sample/s magnetometer data) appears to be predominantly continuous noise. The Pi2 frequency band is denoted by *J* = 3–5, and the Pi1 frequency range by *J* = 5–9. Note that Table 4 denotes that there is significant (but minimized) overlap between the Pi2 and Pi1 frequency bands. For example, the *J* = 5 band represents the longer period Pi1 waves as well as the shorter period Pi2 pulsations. Clear in Fig. 7 is the *J* dependence of the time when power appears above the noise for this substorm onset. In the *J* = 5 frequency band the power appears above the noise at 05:51:48 UT ± 16 s (i.e., 112 s past 0550 UT). Note that the error quoted is an estimate given the size of the temporal resolution; the signal is simply observed during that window, and so we quote the middle value. Using this method, we can establish the onset time at which power in a given *J* rises above the pre-onset noise, as well as determine the frequency band of first signal arrival, for stations across the entire CARISMA and THEMIS GMAG array, as well as in the geosynchronous GOES magnetometer data. From Fig. 3 we apply the Meyer DWT analysis described above, and find that the onset of the Pi1/2 ULF waves in GOES-11 and -12 are clear also (see also the top two panels in Figs. 5 and 6). GOES-11 is situated closer to
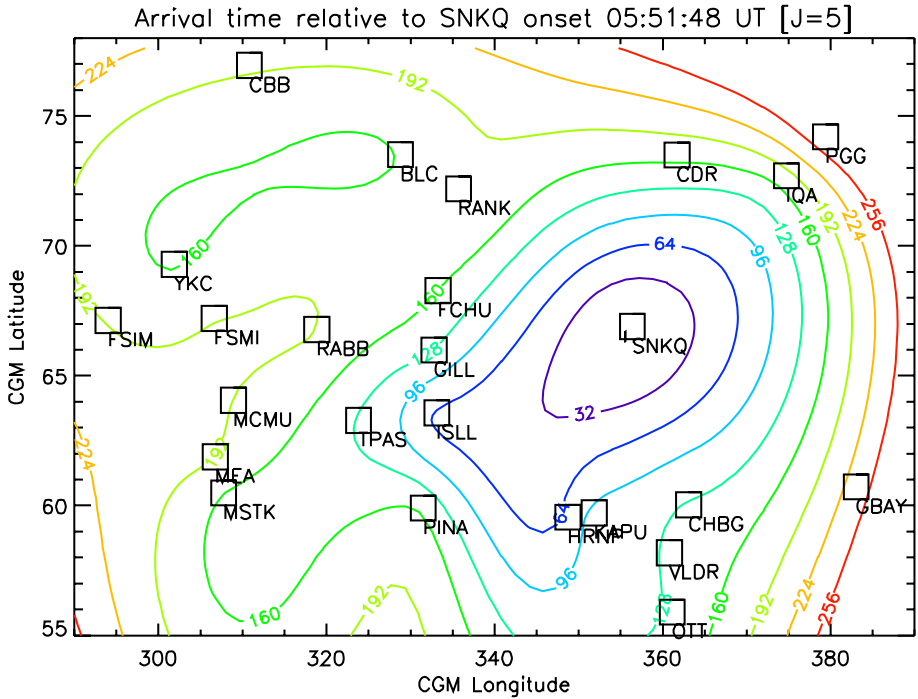
Fig. 8 Contour plot of the spherical harmonic fit to the $J = 5$ DWT first magnetic disturbance arrival time for 25 magnetometer stations across Canada as a function of CGM co-ordinates

the dusk flank (as is the THEMIS constellation) and the onset of the $J = 5$ band is 0556:52 UT $\pm$ 16 s, whereas the onset as defined by GOES-12 is at 0552:04 UT $\pm$ 16 s.

It is remarkable that the signals at SNKQ and observed in-situ with GOES-12 are observed within experimental error of each other. This contemporaneous onset of Pi1/2 signal on the ground and at a closely conjugate satellite in space appears to be too fast to be explained by bouncing of Alfvén wavepackets along the field to establish the magnetosphere-ionosphere coupling; rather, it points to the intriguing possibility that energetic electrons may be their rapid communication mechanism (e.g. Watt et al. 2005).

Figure 8 represents a contour plot of the arrival time of the $J = 5$ wavelet band for the 25 magnetometers used in this study. The contours of equal time are created from a two-dimensional spherical harmonic fit to the $J = 5$ onset times from these stations. Each coloured contour is 32 s apart, and times are shown as seconds since 0551:48 UT, from the initial onset time observed at SNKQ. There is a clear and coherent onset pattern to these $J = 5$ Pi1/2 ULF waves as seen in the ground magnetometer data; the onset of the $J = 5$ Pi1/2 ULF waves occurring first at SNKQ (0551:48 UT), and 64 s later at ISLL and later at surrounding stations (96 s at GILL, 160 s at FCHU, etc.). Since there is a definitive onset location and propagation of the onset of the Pi1/2 signal, the implication is that there must be a physical mechanism which this onset location and propagation pattern is associated with. This will be the subject of future studies, but the initial conclusion may be that this is a signature of the evolution of the magnetospheric source of these pulsations. Note that these propagation times are much faster than the propagation of the maximum Pi1B wave power which Arnoldy et al. (1998) associated with the propagation of the optical auroral substorm

surge. Arnoldy et al. (1998) (see also Posch et al. 2007) also present a by-eye analysis from approximately one hour spectrograms showing a faster "prompt" propagation of lower amplitude Pi1B which starts from a lower latitude station with a large amplitude Pi1B and "promply" propagates, albeit at low amplitude, to higher latitude stations. We believe that the expansion of the onset of Pi1 power in the $J = 5$ Pi1/2 ULF waves presented in Fig. 8 indicates that even the "prompt" Pi1B propagation described by Arnoldy et al. (1998) in fact clearly propagates, both polewards and azimuthally, from a localized low latitude epicenter.

4.2.5 Substorm Current Wedge Location

Evaluating the location of the substorm current wedge is an integral part of the analysis and interpretation of the ground magnetic signals surrounding substorm onset needed to place the location of the THEMIS satellites in context. Figure 9 shows the ground magnetic perturbations obtained when the magnetic bays are estimated using a Biot-Savart law integration of an imposed line current model for the substorm current wedge in an assumed dipolar magnetic field (e.g. Cramoysan et al. 1995). Such a model can be used to locate the elements of the SCW using the magnitude and sign of the bays which are seen across a grid of magnetometer stations. From top to bottom, Fig. 9 shows the H-, D- and Z-component deflections which are expected to be observed by ground magnetometers in response to the model SCW. Superimposed upon these three figures are dashed lines indicating the upward and downward field-aligned current elements (vertical) and electrojet latitude (horizontal) which are assumed in the model. By careful analysis of the initial bay disturbance deflection on the ground across an array of stations, the location of the SCW elements in relation top these stations can be deduced. Note that although this model assumes a dipolar field,

Fig. 9 (Colour online) Magnetic perturbations from the Cramoysan et al. (1995) substorm current wedge model in the (*top*) H-, (*middle*) D- and (*bottom*) Z-component magnetic field deflections. *Red* denotes a positive deflection, whilst *blue* represents a negative deflection. The *horizontal dashed line* denotes the electrojet latitude, and the *vertical lines* denote the (*left*) upward and (*right*) downward field-aligned current elements
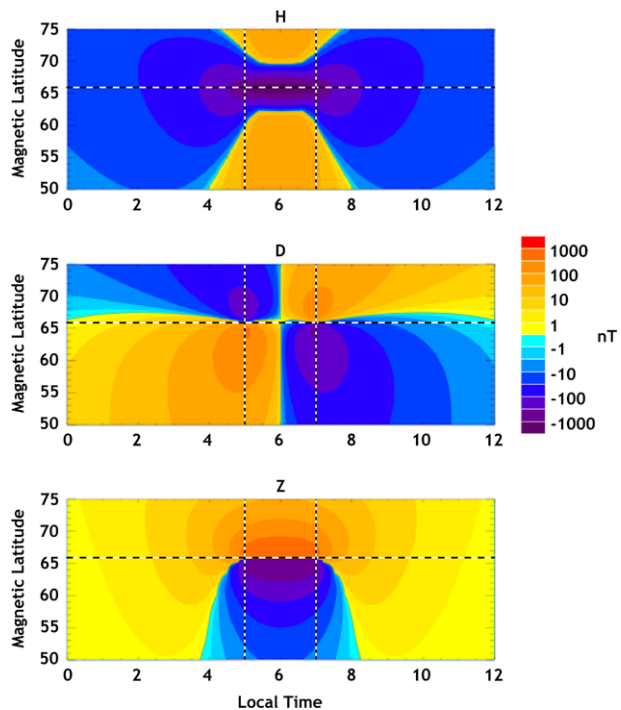
the largest magnetic contributions to the ground signal arising from the Biot-Savart integration occur from the sections of the FAC closest to the ionosphere. Since this region is also likely to be the most dipolar, the assumed dipolar field geometry should not generate any significant errors in the location tool, especially on the scale of the spatial separations of the stations within the array used to locate the SCW. Through best-fit to the observed bays, CARISMA can provide diagnosis of the locations of the latitude of the auroral electrojet, and the longitudes of the upward and downward FAC elements. Such analysis can be completed by the CARISMA team on a collaborative basis in future for the second THEMIS tail season. Locating the SCW elements using this technique across the combined magnetometer arrays shown in Fig. 8 places the meridian of the downward FAC between KAPU and VLDR in the same meridian as SNKQ, the upward FAC element between TPAS and ISLL, and the electrojet latitude between GILL and ISLL. The location of the downward FAC therefore appears to be coincident with the magnetic onset location at SNKQ, suggesting that the downward FAC and the onset initiation process may be intimately linked.

4.3 The Ionospheric Alfvén Resonator

The ionospheric Alfvén resonator (IAR) resonant cavity develops in the topside ionosphere as shear Alfvén waves become trapped in a standing wave pattern between regions of large Alfvén velocity gradients at the cavity boundaries. The induction coil component of the CARISMA expansion will enhance studies of the physics and morphology of the IAR in the Canada–US sector. Interest in the Alfvén resonator (Lysak 1991, 1994; Belyaev et al. 1990) has grown in recent years due to increasing indications that the resonator's effects on plasma dynamics and energy transport through the coupled magnetosphere–ionosphere–thermosphere system are significant.

The excitation of the IAR can be observed as multiple harmonic resonance bands in the 0.1 to 10 Hz range that rise and fall with diurnal changes in upper ionospheric parameters (Hebden et al. 2005; Yahnin et al. 2003). Magnetic fingerprints of the stimulated IAR above Athabasca station ($L = 4.61$) on September 25, 2005, are shown in Fig. 10. Recently, magnetic signatures of the IAR occurring at sites spread across a range of L-shell
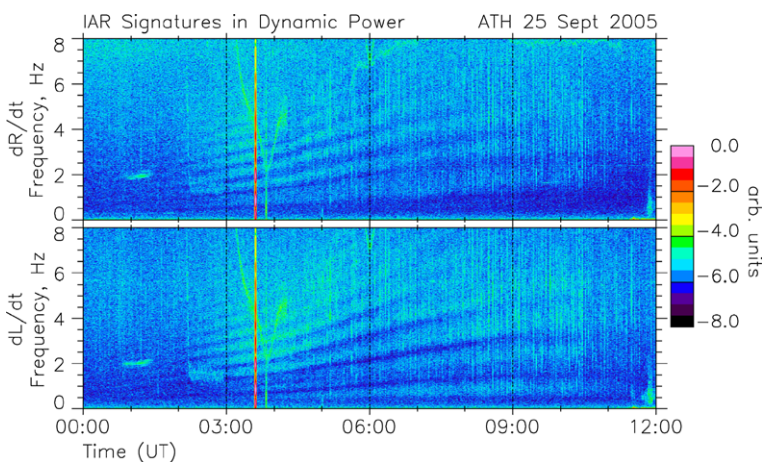

Fig. 10 (Colour online) Magnetic signatures of the IAR recorded in right- and left-hand circularly polarized dynamic power at Athabasca Geophysical Observatory on 25 Sept. 2005. The *color scale* indicates logarithmic power normalized to peak power in each spectrogram

and magnetic local time in the Canada–US sector and Russia have been studied (Parent et al. 2007). However, the excellent time resolution and strategic two-meridian coverage of the new CARISMA induction coil network will allow long-term statistical studies of IAR signatures at multiple stations across Canada.

The relationship between IAR signatures and topside ionospheric parameters can lead to the use of IAR observations as a diagnostic of F-region dynamics, including the ionospheric response during substorms. Particle precipitation during substorm events can disrupt and change the ionospheric plasma density profile in localized areas, thus directly affecting observed signatures of the IAR (Parent et al. 2008, in preparation). CARISMA induction coil observations of the ionospheric Alfvén resonator, along with CGSM riometers and optics, can nicely complement the study of substorm dynamics in the THEMIS era.

4.4 Discussion

In Sect. 4.2 above, we described some of the capabilities of the CARISMA array for substorm studies. These include timing and locating the first evidence of substorm onset waves in the ionosphere, as well as locating the regions of first wave arrival and SCW location. Since the capability to resolve the magnetic signals of substorm onset is not affected by cloud, as is the case for ground-based optics, these capabilities provide a powerful tool for substorm science especially when combined with data from the in-situ THEMIS probes. Specifically, the ionospheric signatures can be used to constrain the competing NENL and current disruption models of substorm onset since these models must ultimately be able to explain the magnetic timing and location observed in relation to the time sequence of events at substorm onset. CARISMA magnetic monitoring can also be used to do substorm science in its own right.

For example, the nature of the drivers of the Pi2 and Pi1 waves which are seen at onset is not fully understood. In general, the nightside magnetosphere during the substorm expansion phase is awash with geomagnetic activity, and it has long since been established that nightside ULF fluctuations are an integral part of the substorm (Saito 1961). However, there are debates as to the generation mechanism and drivers of many of these classes of ULF pulsations. For example, Rostoker et al. (1980) identified that the Pi2 pulsation (40–150 s period) was integral to the substorm process and substorm onset, and could be used to time substorm onset to ∼minute timescales. The Pi2 ULF pulsations are thought to occur in the near-Earth plasmasheet, and field-aligned currents that establish the substorm current wedge (SCW) are established by the field-aligned propagation and ionospheric reflection of the Alfven waves in the Pi2 wavetrain. The characteristic decaying waveform of the Pi2 can therefore be explained by this reflection process (e.g., Baumjohann and Glassmeier 1984), and is observed in ground magnetograms as a series of Pi2 pulsations "riding on" the magnetic bays associated with the currents in the substorm current wedge. However, the Pi2 has since also been attributed to direct driving arising from the impact of earthward propagating of quasi-periodic Bursty Bulk Flows (BBFs; e.g. Kepko and Kivelson 1999; Kepko et al. 2001) or alternatively as a result of natural resonance frequencies in the nightside magnetosphere (e.g. Rae et al. 2007a). The frequencies of the Pi2 must be determined both or one of either the natural frequency content of the CPS disturbance, or the natural frequencies within the near-Earth CPS. Studies of the polarization of the Pi2 (e.g. Lester et al. 1983) have also shown them to be an excellent indication of the location of the substorm current wedge, in terms of location of both the upward and downward field-aligned current elements, and the centre of the electrojet. Furthermore, this can be verified with substorm bay analysis using a simple model for SCW location (e.g., Cramoysan et al. 1995;

Sect. 4.2). Finally, CPS disturbances have been shown to generate compressional fast mode waves, which may impact the plasmasphere and set up compressional plasmaspheric cavity modes (e.g. Allan et al. 1996). We direct the reader to Olson (1999) for a comprehensive review of the Pi2 pulsation. Overall, either the NENL model or the current disruption model must be able to explain both the relationship of these waves to the physical drivers arising from the processes during the expansion phase, as well as being able to explain their timing in relation to the sequence of events at onset.

The increase in temporal resolution and spatial coverage of the ground magnetometry has led to the discovery of higher frequency ULF waves associated with substorm on-set. The Pi1 (1–40 s period) class of ULF wave is comparatively much less studied than those waves in the Pi2 band, and their relationship to onset processes much less well un-derstood. If Pi1 waves are consistently observed before or even at the same time that the Pi2 is established, then it should be possible to time substorm onset with ground magne-tometry to an increased accuracy due to the smaller wave periods in the Pi1 band. It is often stated that the first signature of substorm onset is the brightening of the auroral sig-nature in optical measurements (e.g. Mende et al. 2007). However, the possibility of using Pi1 techniques may allow the relationship of Pi1s to the onset process to be determined. Moreover such timing could be done during cloudy conditions (e.g., Milling et al. 2008; Murphy et al. 2008; Rae et al. 2008a, 2008b). There is already some evidence that Pi1 sig-natures might be more local than Pi2s (e.g. Posch et al. 2007). The initial results from the DWT analysis also suggests that this might be the case, the results in this review already indicating the likely utility of Pi1s for both local substorm onset location and indeed for increased accuracy timing. Interestingly, broadband Pi1 signals in the 0.1–10 s period range known as Pi1Bs have also recently been studied in space and on the ground (e.g. Lessard et al. 2006). These signals may also provide a new window on the onset process, especially since one hypothesis suggest that Pi1Bs might be generated by FAC instabilities (see e.g. Lessard et al. 2006 and references therein). The long-period Pi1 waves which appear to pro-vide a coherent substorm onset timing (cf. our Figs. 7 and 8) appear to be related to the location of the downward FAC (Milling et al. 2008). However, further studies are needed to establish their causal driver and their relation to the spatial and temporal development of process(es) operating during expansion phase onset.

5 Dayside Science Capabilities

One of the excellent scientific capabilities of the in-situ THEMIS orbits is their design to return to a meridional telescopic alignment once every four days. In the nightside this ca-pability is designed for substorm science, but on the dayside it provides the capability to monitor the upstream solar wind as well as energy and processing of solar wind distur-bances by the bow shock and magnetopause, and their ultimate role in energy transport into the dayside magnetosphere. As discussed in Sect. 3.2, this provides a unique capability for answering dayside science questions (the THEMIS tertiary objective), especially since in the prime mission phase the orbits of the THEMIS probes come into telescopic alignment over the Canadian sector both during tail (northern hemisphere winter) and dayside (north-ern summer) observing seasons, as well as on the magnetospheric flanks during the periods in-between.

The excitation of global scale ULF waves and field line resonances (FLRs) (see e.g. the review by Wright and Mann 2006) is increasingly recognized as an energetically significant component of solar-terrestrial energy transport (cf. Greenwald and Walker 1980). For exam-ple, at times the total energy deposited via ionospheric Joule heating due to Pc5 ULF waves

may reach up to ∼30% of the energy deposited during a substorm cycle (see also Rae et al. 2007b). Dayside long period Pc3–5 ULF wave modes can be classified by their external or internal excitation mechanisms into groups with high or low azimuthal wavenumber (m) (see e.g. the review by Hughes 1994). Nightside ULF waves, although critical for energy transport and diagnosing tail dynamics, are particularly poorly understood. Due to their energetic significance, and their role in transporting energy and coupling different energy plasma particle populations, ULF waves are an important research focus for CARISMA.

Below, we concentrate on highlighting the capabilities of CARISMA for completing studies of the solar wind excitation of dayside ULF waves, especially by solar wind impulses and through the development of magnetopause Kelvin-Helmholtz instabilities, as well as studies of the internal excitation of ULF pulsations by energetic ions. By analyzing the longitudinal phase change of a ULF wavepacket, the waves' azimuthal wave number, m, can be determined and hence these two populations of waves can be separated using ground-based magnetometer data (see e.g. Chisham and Mann 1999).

5.1 Excitation and Propagation of Low-m ULF Pulsations

The role of discrete frequency cavity/waveguide modes in the injection of low-m ULF energy into field line resonances (FLRs) in the magnetosphere is now on a strong theoretical (e.g. Samson et al. 1971; Kivelson et al. 1984; Kivelson and Southwood 1985; Wright 1994; Mann et al. 1999; Walker 2000) and experimental footing (e.g. Samson et al. 1992; Walker et al. 1992; Ruohoniemi et al. 1991; Mann and Wright 1999; Mathie et al. 1999a, 1999b; Mathie and Mann 2000a, 2000b, 2000c). The amplitude of the wave peaks at the location of the FLR and the phase of the wave changes with latitude by 180° across the FLR. Figure 11 illustrates these FLR features (cf. Samson et al. 1971) measured on the ground by the Churchill latitudinal array of CARISMA magnetometers (see Rae et al. 2005 for more details).

Solar wind discontinuities, pressure pulses, buffeting, as well as the Kelvin-Helmholtz instability (KHI) at the magnetopause (see the schematic in Fig. 12) have all been proposed as drivers for cavity/waveguide modes (e.g. Allan et al. 1986; Mann et al. 1999, 2002; Mann and Wright 1999; Mathie and Mann 2001; Rae et al. 2005). Pc5 ULF power, especially in the dawn sector, is also strongly correlated with solar wind speed (e.g. O'Brien and McPherron 2003; O'Brien et al. 2003; Mathie and Mann 2001; Mann et al. 2004). However, detailed studies are required to establish the dominant mechanisms of long-period ULF wave excitation in the dayside magnetosphere. Indeed, the detailed ULF wave response in the magnetosphere to fast solar wind streams, co-rotating interaction regions (CIRs), interplanetary coronal mass ejections (ICMEs), are not well-known.

The KHI is most likely to excite ULF waves during fast solar wind (>700 km/s) intervals, perhaps preferentially in the morning sector where the statistically the Parker spiral interplanetary magnetic field is approximately perpendicular to the Earth's magnetopause boundary. Figure 13 shows L-MLT maps of the 1–10 mHz integrated ULF amplitude for low (<300 km/s), medium (500–600 km/s) and high (>700 km/s) solar wind conditions using 10 years of CARISMA data from 1996 to 2006 for the H- and D-components observed on the ground, and mapped to the equatorial plane assuming a dipole field. The results presented in Fig. 13 clearly illustrate that ULF wave power increases with solar wind speed and that there is much more ground-based ULF wave power in the dawn sector compared to the dusk sector. The enhanced and localized H-component ULF wave power in the dawn sector is most likely caused by guided toroidal FLRs resulting from compressional waveguide modes excited by the KHI at the magnetopause boundary under fast solar wind conditions. The
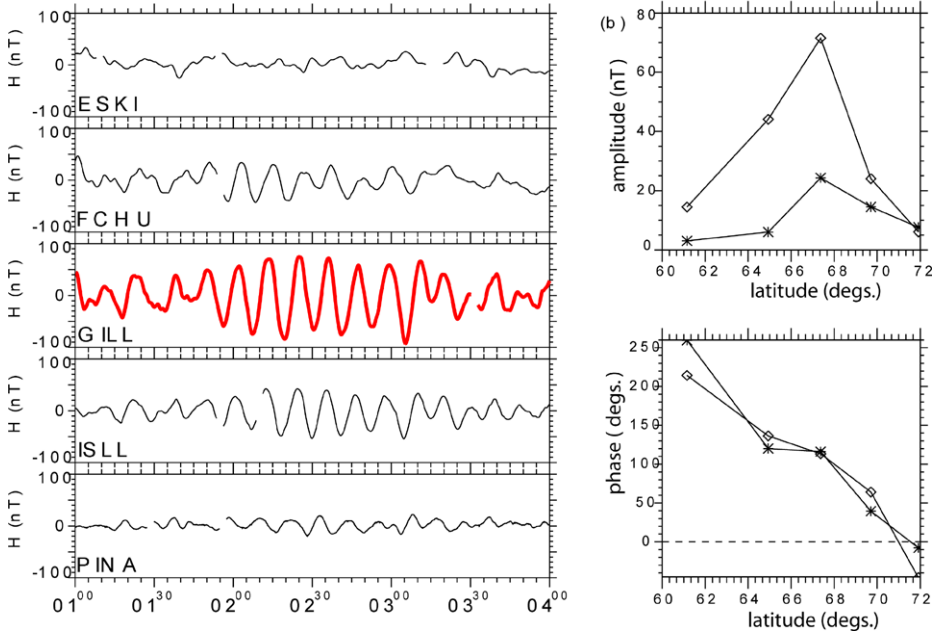
25 Nov 2001: CANOPUS magnetometer array

Fig. 11 (**a**) Unfiltered H-component ground magnetograms from the "Churchill line" of CARISMA magnetometer array between 0100 and 0400 UT on 25 November 2001. (**b**) Complex demodulation of the H-(*diamonds*) and D-(*stars*) components of the dominant spectral peak (i.e., 1.5 mHz) taken at 0235 UT. The *top* and *bottom panels* of (**b**) represent the amplitude and phase along the "Churchill line" of magnetometers. Adapted from Rae et al. (2005)
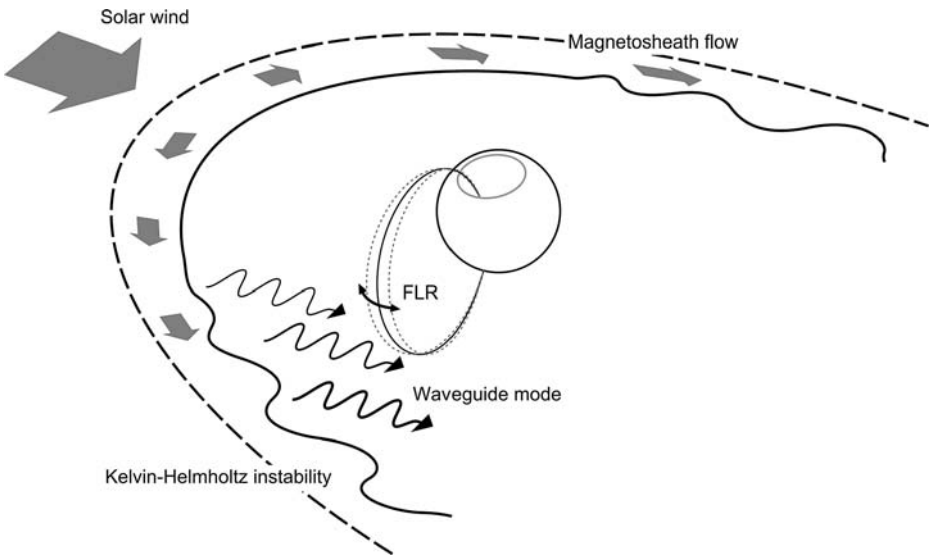
Fig. 12 Schematic showing the excitation of a field line resonance by compressional waves driven by magnetopause Kelvin-Helmholtz instability on the flanks of the magnetosphere. Taken from Rae et al. (2007b)
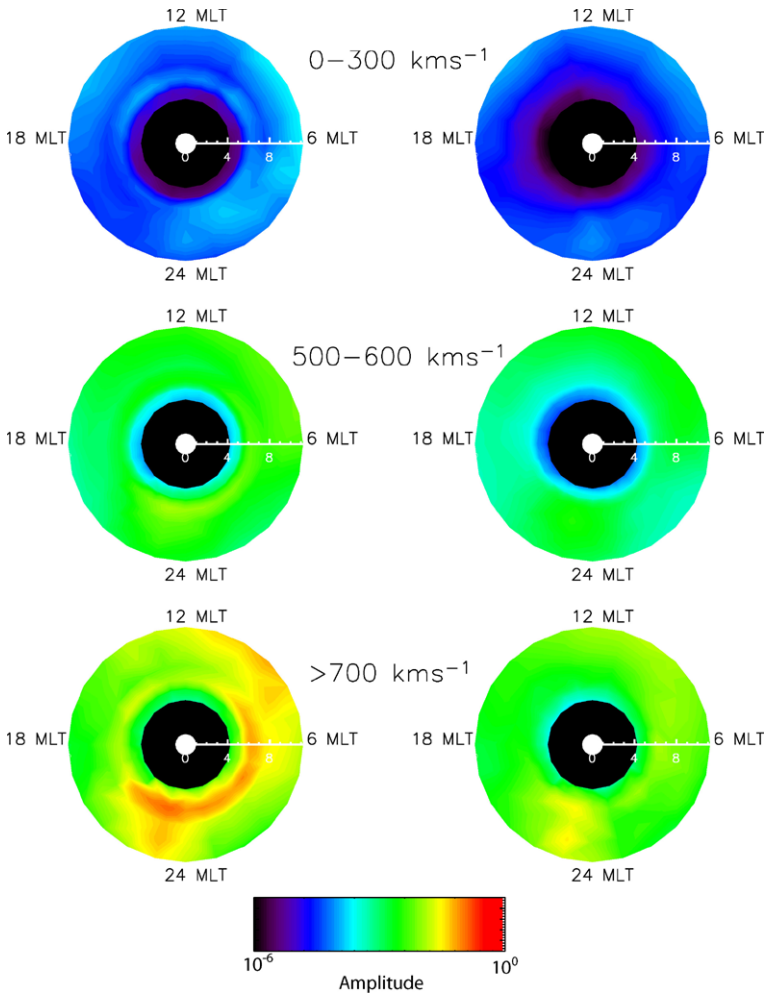
Fig. 13 Amplitude maps of 1–10 mHz frequency integrated ULF amplitude spectra for low (<300 km/s), medium (500–600 km/s) and high (>700 km/s) solar wind conditions, for the H-component (*left column*) and D-component (*right column*) from the Churchill line magnetometers at PINA, ISLL, GILL, FHCU, and RANK. The plots were produced using 10 years of CARISMA data from 1996 to 2006

field line resonance signature is strongest in for stations with L-values in the auroral zone in the H-component, and has a significantly lower amplitude at the lowest L-value station in the plot (PINA). A similar field line resonance signature can be seen in the D-component, but at much smaller amplitude. It is also interesting to note that this auroral zone FLR amplitude enhancement is strong in the morning sector, but extends around the nightside into the pre-midnight sector. There is also evidence for a pre-midnight H-component power enhancement which crosses all L-shells and is especially clear at high solar wind speeds. We believe that his may be evidence for tail waveguide modes (see e.g. Wright and Mann 2006, and references therein). Finally, in the pre-dawn sector there is evidence for an MLT localized H-component power feature which is confined predominantly from the pre-noon to the dawn sector, and whose amplitude decreases with decreasing L. We believe that this is

likely a signature of the waveguide modes, or of magnetopause KHI surface waves, driving the observed FLR response. Future work combining the observed ground signatures with data from the in-situ THEMIS probes will be very useful for establishing the nature of the in-situ disturbances corresponding to these features on the ground.

The dominance of a field line resonance response in the morning sector over the afternoon, as seen by ground-based magnetometers, remains a puzzle. Previous research has suggested that potential explanations include stabilizing magnetic field tension at dusk (e.g. Miura 1992) or the comparative lack of seed perturbations for the KHI downstream of the quasi-perpendicular shock which for Parker spiral IMF orientation is on the dusk side (see e.g. Lee and Olson 1980). More recently, Glassmeier and Stellmacher (2000) suggested that the local time asymmetry of the radial gradients in plasma density around the dayside magnetosphere due to refilling might also preferentially screen Pc5 FLRs from the ground in the dusk sector. Finally, Rostoker and Sullivan (1987) suggested that different field line resonant responses might be generated either side of local noon because of the MLT dependence of the characteristics of driving solar wind disturbances. Specifically, Rostoker and Sullivan (1987) suggested that since solar wind dynamic pressure pulses impact the early afternoon magnetopause, these authors finding that the afternoon-side ULF wave response was more closely associated with solar wind impulses than that on the morning-side. However, more studies combining large scale latitudinal and longitudinal FLR characterization together with conjugate multi-point in-situ measurements such as those which are available with the THEMIS probes provide a capability to begin to solve this puzzle.

Another enigma is that there is often very little in-situ observational evidence of compressional waveguide modes of significant amplitude (e.g. Anderson and Engebretson 1995; Waters et al. 2002). Multiple satellites have seen the downtail propagation of waveguide modes (e.g. Mann et al. 1998), however, the number of such examples is limited. Further simulation studies have also suggested that due to dispersion down the magnetospheric waveguide, waveguide mode harmonics may not display quasi-sinusoidal signatures in the time domain at a single location, making them potentially difficult to identify in satellite time-series data (Rickard and Wright 1995). Multi-point studies with THEMIS can examine the waves in the magnetosphere at the times of well-defined CARISMA observed FLRs, as well as the nature of fluctuations at the magnetopause (e.g. Mann et al. 2002; Rae et al. 2005) and even in the sheath and solar wind, especially on the flanks. THEMIS conjunctions to CARISMA offer the ideal capabilities for these studies, especially during the early mission "string-of-pearls" configuration. Multi-point satellite studies could establish causality from studies characterizing directions of energy flow, magnetopause thickness, and magnetopause oscillation amplitudes. These could encompass studies of the role of the IMF in stabilizing the KHI, the role of direct coherent driving (cf. Kepko and Kivelson 1999) versus natural waveguide mode harmonic resonances (cf. the simulations of Wright and Rickard 1995), the role of the magnetopause over-reflection mechanism (e.g. Mann et al. 1999), and the role of non-linear KH vortex development (cf. Hasegawa et al. 2004; Fairfield et al. 2007), and the potential role of seed magnetosheath fluctuations downstream of the bow shock (e.g. Miura 1992).

5.2 Excitation and Propagation of High-m ULF Pulsations

Ring current ions injected into the magnetosphere naturally evolve as the ions drift and bounce through the inner magnetosphere. The energy and pitch angle dependence of the drift trajectories, including the effects of convection electric fields as well as magnetic gradient and curvature drifts, can generate spatial and energy gradients leading to a fundamental

plasma instability where ion energy is transferred into guided high-m poloidal ULF waves in the Pc4–5 range especially through the drift-bounce resonance mechanism (e.g., Hughes et al. 1978; Southwood et al. 1969; Southwood 1976; Southwood and Kivelson 1982; Ozeke and Mann 2001). High-m waves are seen extensively in the local afternoon sector along ion injection paths from the tail during the main phase of geomagnetic storms (e.g. Cao et al. 1994, and Anderson et al. 1990), however, there are relatively few ground-satellite conjunction studies showing definitive evidence for free energy transfer to the waves.

Theory suggests that the drift-bounce resonance instability, and related diamagnetic drift, drift-mirror, and drift-Alfven ballooning modes (e.g. Chen and Hasegawa 1991; Vetoulis and Chen 1994) could explain the high-m poloidal waves observed. Observations capable of distinguishing between proposed excitation mechanisms are rare. Some statistical studies of the free energy in bump-on-tail distributions have been completed (e.g. Baddeley et al. 2004), yet debate remains about whether this loss process from the ring current is energetically significant (e.g. Wilson et al. 2006). Even for the simpler case of giant pulsation excitation, which typically occurs during quiet times likely also by drift-bounce resonance, debate continues (e.g. Chisham et al. 1992, 1997). The equatorial multi-point configuration of THEMIS, conjugate to CARISMA, offers the ideal vehicle with which to determine the physical mechanisms exciting these waves, and their role in ring current loss. Supporting measurements from other CGSM ground-based arrays, and partner satellite energetic particle observations especially resolving distribution function evolution along ion drift path, will aid science closure.

6 Radiation Belt Science Capabilities

One of the most interesting and important questions in current solar-terrestrial physics research concerns the acceleration of electrons to relativistic speeds. The fundamental mechanisms proposed to explain the dynamics, energization and loss of these particles are numerous, and which dominate remains largely unknown (see e.g. the review by Friedel et al. 2002). Likely the most influential acceleration mechanisms are resonance with VLF lower band chorus, which operates through violation of the first adiabatic invariant (e.g. Meredith et al. 2003; Chen et al. 2007, and resonance with ULF waves which typically operates through violation of the third (e.g. Fälthammer 1966; Schulz and Lanzerotti 1974; Elkington et al. 2002). Together with in-situ THEMIS measurements of both ULF wave electric and magnetic fields as well as energetic electron flux up to 900 keV with the solid state telescope (SST; see McFadden et al. 2008), CARISMA has an excellent capability for supporting studies of ULF wave related radiation belt acceleration and loss processes and hence to the secondary objective of the THEMIS mission. Indeed, having 5 probes provides an excellent capability to resolve the spatial and temporal structure of the evolution of energetic electron flux and phase space density during magnetic storms.

6.1 Pc5 ULF Wave Drift-Resonant Acceleration

Recent theoretical and observational developments have highlighted the possibility that Pc5 ULF waves might accelerate electrons to MeV energies in the outer radiation belt through drift-resonance (e.g. Rostoker et al. 1998; Elkington et al. 2002, 2003; Hudson et al. 2000; Mathie and Mann 2000c, 2001; O'Brien et al. 2001; Mann et al. 2004). Mathie and Mann (2001), showed clear correlations between daily dawn-side Pc5 ULF power and both solar wind speed and >2 MeV electron flux at geosynchronous orbit (GEO) for 6 months of the declining phase of the solar cycle in 1995.

Evidence in favor of longer timescale stochastic ULF wave radial diffusion also comes from ULF wave correlated MeV electron flux having even being shown to statistically propagate radially inwards from $L = 6.6$ to $L = 4.5$ (Mann et al. 2004). Historically, collisionless radial diffusion coefficients (e.g. Fälthammer 1966; Schulz and Lanzerotti 1974) have been quantified as a function of Kp from observations such as from CRRES (e.g. Brautigam and Albert 2000). Despite their simplicity, these have been able to generate models which reproduce many of the global morphological features of the radiation belts (e.g. Shprits et al. 2005; Mai Mai Lam and Richard Horne, Personal Communication 2007). The diffusion coefficient formalism developed by Brizard and Chan (1999, 2001, 2004) which derives the diffusion coefficients as a function of wave power at frequency $\omega = m \, \omega_d$, for 90° pitch angle particles in an uncompressed dipole field, can be used with the CARISMA magnetic field power to produce data driven energy dependent radial diffusion coefficients, once mapping from the ground measurements to the equatorial magnetosphere is computed (e.g. Ozeke et al. 2008). Such diffusion model studies can also look for regions where additional sources such as VLF acceleration are required.

The unusual MeV electron penetration into the slot region during the first day of the Halloween 2003 storms (e.g. Baker et al. 2004) was shown by Loto'aniu et al. (2006) to be consistent with enhanced ULF wave radial diffusion occurring in response to ULF wave penetration to anomalously low-L. On the 29th October 2003, a rapid decrease in eigenfrequency was observed using the cross-phase technique (see Sect. 6.3), most likely due to the injection of O^+ ions from the ionosphere, enabling ULF wave energy to penetrate much more deeply than usual (Loto'aniu et al. 2006; Kale et al., in preparation). Tantalisingly, this suggests that cold (eV energy) plasma might play a critical role in the dynamics of the apparently totally separate MeV energy radiation belt particle population, 6 orders of magnitude away in energy, via the intermediary of ULF waves. Recent studies have also suggested that eastward propagating moderate azimuthal mode waves ($m \sim 20$–40) (cf. Sect. 5.2), driven by drift-bounce resonance with ∼few 100 keV O^+ ions outside a depleted plasmapause, can also energize MeV electrons via drift resonance at $L \sim 4$ (Ozeke and Mann 2008). Given there is an ample supply of energy in the ring current, such a mechanism is attractive for radiation belt electron acceleration. More case and statistical studies are required to validate these important concepts.

Recent studies completed by the CARISMA team have also shown the strong time domain coherence between ULF wave oscillations seen on the ground and modulation of energetic particle flux in a specific ULF wave packet (e.g. Mann et al. 2007). Simulations using the code described by Degeling et al. (2007) were able to reproduce the observed several hundred to ∼1 MeV flux modulation, including a phase change as a function of energy we believe indicates a resonant response. One element of importance will be a careful consideration of the effects of mode polarization on any radiation belt response since poloidally polarized Alfvén modes should be dominated by azimuthal electric fields in the magnetosphere which can strongly interact with the azimuthal drift motion of radiation belt electrons. Conversely, toroidally polarized modes which are usually larger amplitude are expected to display a weaker interaction. Further studies are required including not only polarization, but also more realistic wave models including local time dependence. ULF wave data from CARISMA can be compared in time domain case studies to energetic particle data from THEMIS SST (up to 900 keV), as well as to those available from Polar, Cluster, HEO, SAMPEX, LANL and GOES satellites. Predictions from ULF wave-particle models which utilize tracing of Liouville trajectories in ULF fields (e.g. Degeling et al. 2007) also enable the results to be observationally tested in detail.

6.2 Electromagnetic Ion Cyclotron (EMIC) Waves

Continuous magnetic field fluctuations in the frequency range from 0.2 to 5 Hz are classified as Pc1 pulsations (Jacobs et al. 1964). Waves in the Pc1 band can be driven by the electromagnetic ion cyclotron (EMIC) instability, where free energy is provided by hot equatorial ions with temperature anisotropy ($T_{perp} > T_{par}$). Depending on ion composition, EMIC waves occur in three bands below the hydrogen, helium and oxygen ion gyrofrequencies. Despite satellite and ground observations since the 1960s, EMIC waves are still somewhat poorly understood; multi-point THEMIS and continent scale CARISMA observations provide the capability to examine the excitation processes, and the space-ground propagation characteristics, including the effects of ducting in the Earth-ionosphere waveguide (e.g. Fraser 1976). In the inner magnetosphere, EMIC waves are believed to be preferentially excited in a spatially localized zone along the high density dusk-side plasmapause, occur most frequently and are the most intense during magnetic storms (Horne and Thorne 1993; Kozyra et al. 1997; Jordanova et al. 2001), but in the outer magnetosphere have an occurrence rate which increases with L towards the magnetopause and are present even during very quiet geomagnetic conditions (see Anderson et al. 2002; Engebretson et al. 2002).

On the ground, EMIC waves are often observed as structured pulsations, which appear as sequence of discrete dispersive wave packets with repetition period of a few minutes (e.g. Mursula et al. 1997), while in space EMIC waves are typically unstructured: only a few cases of satellite observations of structured Pc1 pulsations have been reported so far. Of particular interest is debate about the mechanisms which generate structured Pc1 pulsations. Traditionally, structured Pc1's have been explained by a bouncing wavepacket (BWP) model (e.g. Jacobs and Watanabe 1964), in which a wavepacket travels along the magnetic field line between the conjugate hemispheres and compensates energy losses at the equator. However, observations of the Poynting flux of EMIC waves with the CRRES satellite (Loto'aniu et al. 2005) show that the Poynting flux propagates unidirectionally away from the equatorial plane, contradicting the BWP theory. Figure 14 illustrates the structure of EMIC waves observed simultaneously in space by the THEMIS E satellite and on the ground by the MCMU magnetometer located at ∼30° west of the spacecraft's footprint. According to the BWP model, the ground EMIC waves should have a periodicity in space which is half that seen on the ground. Figure 14 shows an example where the relationship between wavepacket repetition period predicted by the BWP hypothesis is clearly not seen, and the observed wavepacket periodicities appear to be very similar both on the ground and in space (see Usanova et al. 2008 for detailed analysis).

Theoretical investigations have suggested that a Doppler shifted gyroresonant interaction between EMIC waves and MeV energy outer radiation belt electrons can lead to pitch-angle scattering and radiation belt electron loss into the atmosphere (e.g. Summers and Thorne 2003). Outer radiation belt MeV electrons typically drift around the Earth on time-scales of the order 5–10 min and spend only a small fraction of each orbit within the region of EMIC activity. While typical EMIC amplitudes usually exceed the level required for strong diffusion, because of the limited extent of the region of enhanced EMIC activity significant electron loss only occurs over many drift orbits. Under certain conditions (electron plasma frequency/electron gyrofrequency ≥ 10), MeV electrons can be removed from the outer radiation belt over a time-scale of several hours to a day (Summers and Thorne 2003). Such conditions are satisfied within the region of high plasma density and low magnetic field, such as the duskside plasmasphere or detached plasma regions at high L-values.

Despite the potential importance of EMIC waves for radiation belt loss, there are relatively few studies which examine this relationship. Meredith et al. (2003) performed a
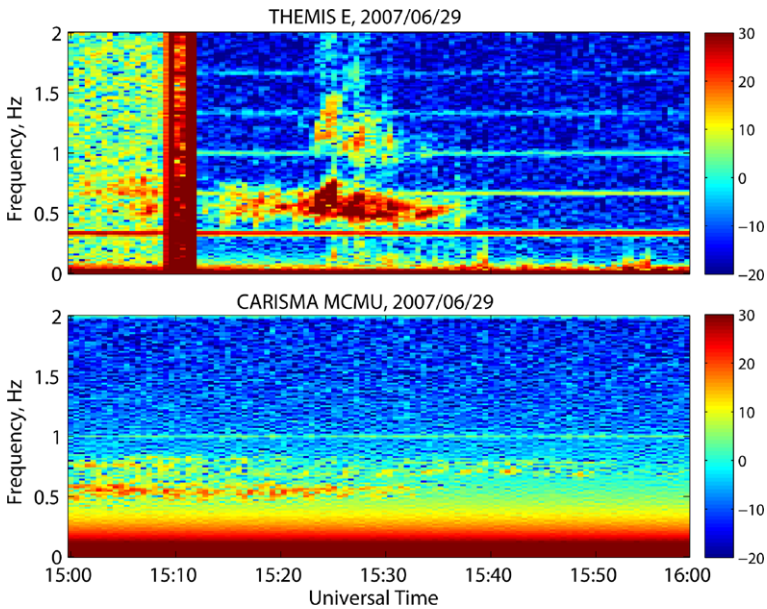
Fig. 14 Fourier spectrograms showing structured Pc1 pulsations detected in space by THEMIS E panel (**a**) and on the ground at the CARISMA MCMU magnetometer station ($L = 5.23$) panel (**b**)

statistical analysis of over 800 EMIC wave events observed on board the CRRES satellite, to establish whether the resonant scattering can occur at energies ≤ 2 MeV. The results of their analysis are consistent with the theoretical study of Summers and Thorne (2003). It has also been inferred from balloon observations of X-ray emissions in the dusk sector that EMIC waves can cause precipitation of MeV energy electrons (Foat et al. 1998; Millan et al. 2002) usually during storm recovery phase.

Further studies to establish the localization of EMIC waves in space, their propagation to the ground, and their potential role in MeV electron loss are required. Partner measurements of MeV electron precipitation loss from low altitude satellites such as NOAA, from balloons (e.g. the NASA funded BARREL project), or inferred from ground VLF networks (e.g. AARDVARK and SID/AWESOME) or even from riometer networks (e.g. from CGSM Norstar riometers) may be important. Ultimately, a characterization of EMIC waves as a function of L, MLT, and geomagnetic activity or storm phase could be used as an empirical input to loss modules within global models for radiation belt dynamics. At present there is a peculiarity that most MeV electron loss in the radiation belts occurs during main phase, yet on the ground EMIC power typically only appears during the recovery phase (e.g. Engebretson et al. 2008; Bortnik et al. 2008 and references therein). Whether this is due to internal reflection of EMIC waves in the magnetosphere (e.g. Rauch and Roux 1982), absorption, perhaps in the presence of heavy ions during the main phase (Horne and Thorne 1994), due to changes in reflection and transmission characteristics of a perturbed ionosphere (Mursula et al. 2000) or represents a lack of waves in the magnetosphere at the times when most MeV electron loss is observed is not clear. Waves below the He^+ gyrofrequency are found to be the most efficient for MeV electron scattering (Summers and Thorne 2003; Meredith et al. 2003), and a superposed statistical survey of EMIC wave power and radiation belt energetic electron flux as a function of L during storms would be valuable.

6.3 Role of the Plasmapause and Plasmasphere

The plasmasphere consists of cold ions and electrons with energies ∼1 eV, which corotate with the Earth. Interestingly, the outer boundary of the plasmasphere, the plasmapause, is believed to have a strong influence on the dynamics of the outer radiation belt's MeV electrons. Li et al. (2006) showed that the lowest L-shell which the outer radiation belt electrons can penetrate to is closely related to the minimum plasmapause location. Several different mechanisms may explain why the plasmapause location affects the penetration of the radiation belt electrons:

- The location of the plasmapause may affect how close to the Earth compressional fast mode waves can propagate inward. If these waves transport the electrons inward via ULF wave driven diffusion or coherent drift-resonance transport (Degeling et al. 2007), then these radial transport mechanisms would be affected by the location of the plasmapause.
- The radiation belt electrons may also be accelerated inward of a drift-resonance region by a guided poloidal FLR, which in turn is generated by an unstable ion distribution. These guided poloidal waves, which are able to resonantly accelerate the radiation belt electrons, are most likely to occur close to a depleted plasmapause (see Ozeke and Mann 2008).
- The electrons in the radiation belt may be locally energized by VLF waves which are most likely to occur in a region just outside the plasmapause (see Horne et al. 2005 and Shprits et al. 2006).

The explanation for the recent observation that the inner edge of the radiation belt is correlated with the plasmapause (e.g. O'Brien and Moldwin 2003; Li et al. 2006; see also Tverskaya et al. 1986) is hence still an enigma. Perhaps the explanation is that VLF acceleration operates just outside the plasmasphere, and losses internal to the plasmasphere remove any particles which diffuse inward across the plasmapause. Alternatively, if a large element of radiation belt morphology is determined by inward (and outward, e.g. Shprits et al. 2004, 2005) diffusion, then perhaps the penetration of ULF wave power such as that described by Loto'aniu et al. (2006) plays an important role. Comparing CARISMA observed ULF power, the cross-phase determined plasmapause location, and energetic particle flux from the satellites described above, would allow the role of ULF waves in producing the observed correlation to be investigated.

Recent observations (Fraser et al., personal communication 2007) using high resolution GOES magnetometer data have also demonstrated a link between EMIC waves and the extension of the plasmasphere into a dayside drainage plume. Other studies have also suggested a link between EMIC waves excited in dense plasma regions and sub-auroral red (SAR) arcs (e.g. Spasojević et al. 2004). Using the CGSM optical and precipitation infrastructure, the generation of SAR arcs could also be addressed using the combination of THEMIS probe and CARISMA infrastructure.

6.3.1 Diagnosing the Plasmapause and Plasmasphere with CARISMA

The plasmasphere was first discovered using ground-based VLF measurements of plasmaspheric ducts (Carpenter 1963). Despite several decades of study from the ground, and onboard satellites (e.g. Boskova et al. 1993; Park 1974) the basic rates of plasmaspheric refilling and the processes responsible are not well-understood, the problem being compounded by the fact that often satellite low energy ion detectors are "blind" to very cold ions due to spacecraft charging. The CARISMA research team and collaborators have been instrumental in developing cross-phase and related techniques for remote-sensing the distribution

Fig. 15 Schematic illustration of the cross-phase technique. Panels (**a**) and (**b**) show the amplitude and phase response of two latitudinally separated magnetometers. Panels (**c**) and (**d**) show the amplitude and phase difference between the two magnetometers
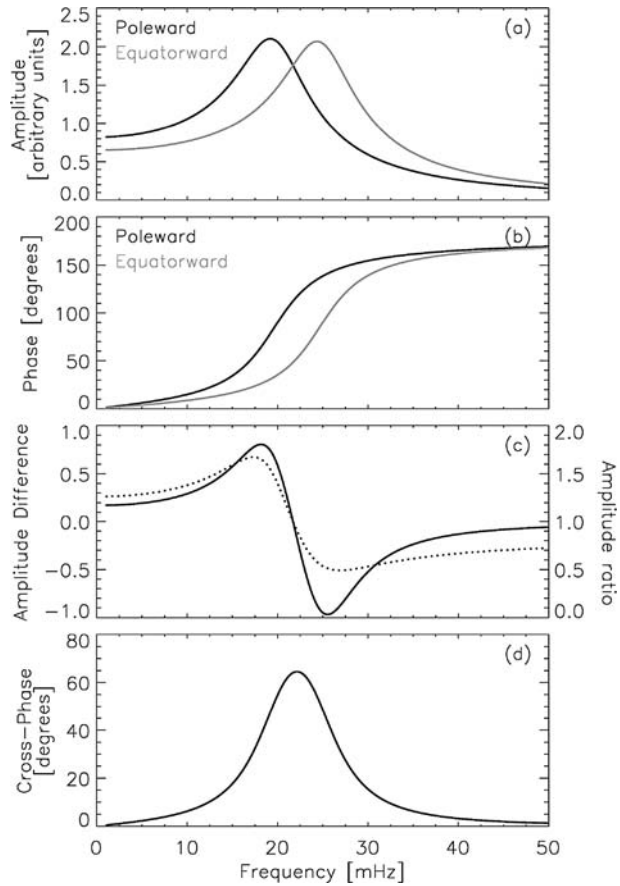
and dynamics of cold plasma using networks of ground-based magnetometers (e.g. Menk et al. 1999, 2000, 2004; Milling et al. 2001; Dent et al. 2003, 2006; Kale et al. 2007). By employing data from ground-based magnetometer networks, it is possible to determine both the location of the plasmapause and the equatorial density profile as a function of L-shell, via detection of local field line eigenfrequencies with the cross-phase technique.

The cross-phase technique examines the H-component amplitude and phase spectra from two latitudinally separated ground-based magnetometers in order to determine the eigenfrequency of a field-line with a foot-point assumed to be near the latitudinal and longitudinal midpoint between those two magnetometers (Waters et al. 1991). Gough and Orr (1984) explained that driven Alfvén waves may be treated as forced, damped simple harmonic oscillators. Figure 15 is based on Fig. 1 of Waters et al. (1991) and presents simple calculations of the response of forced, damped simple harmonic oscillators with eigenfrequencies of 20 mHz and 25 mHz, which represent the field lines at the locations of two latitudinally separated magnetometer stations. The top two panels show the amplitude and phase response as a function of frequency for each of the field-lines. These show the amplitude peak and 180° phase change, which are expected as the frequency passes through resonance. The resonance frequency of the field-line with a foot-point midway between the foot-points of the two field-lines being modeled is identified where the amplitude difference = 0, and am-
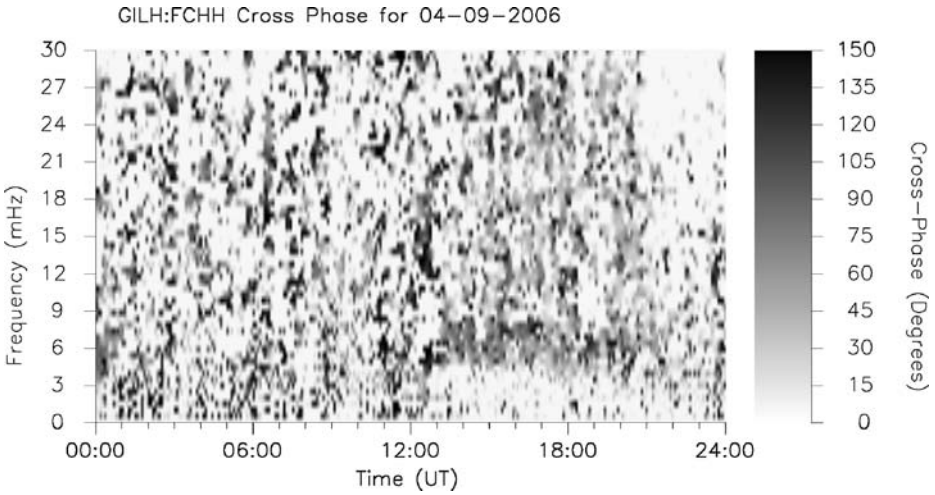
Fig. 16 Dynamic cross-phase spectra for the GILL-FCHU station pair, which belong to the CARISMA array

Fig. 17 (**a**) Fundamental mode field line eigenfrequencies as a function of L-shell, determined using the cross phase technique. (**b**) Equatorial plasma mass densities inferred from the eigenfrequencies presented in panel (**a**)
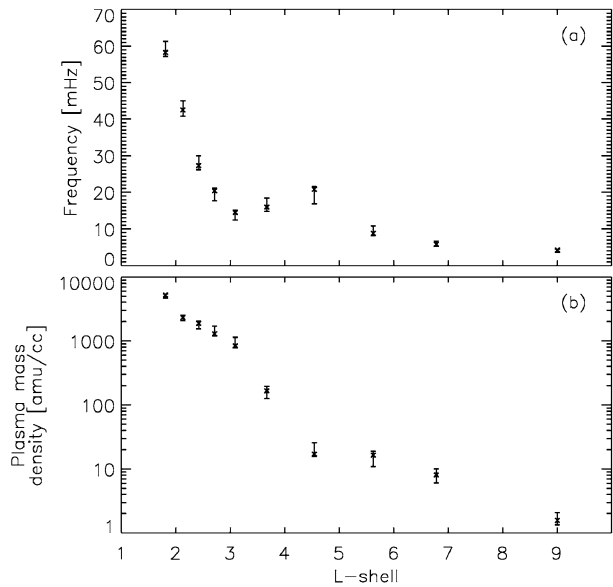
plitude ratio $= 1$ (both with negative gradient), and the cross-phase shows a local maxima at a value >0 (i.e., the phase difference maximizes with a positive value).

Figure 16 shows an example dynamic cross-phase spectrogram, which is plotting the cross-phase (i.e. phase difference) between two magnetometer data sets as a function of frequency and Universal Time. The cross-phase peak, representing the field-line eigenfrequency of the mid-point field-line, is shown by the dark band between ~ 5 and 8 mHz, between ~ 13 and 20 UT.

An example of the capability of ground-based magnetometers to diagnose eigenfrequency and density profiles in the North American sector is shown in Fig. 17. Data from

magnetometers belonging to the CARISMA (4.54 < L_midpoint < 9.00) and McMAC (Mid-Continent Magnetoseismic Chain; 1.50 < L_midpoint < 3.09) ground-based magnetometer arrays have been employed. This example shows data from 4 September 2006, between 1700 and 1800 UT. The plasma mass density values have been determined assuming a dipolar magnetic field geometry, and a radial density variation $\propto r^{-1}$ along the field-lines (described in more detail in Dent et al. 2006). The error bars represent the uncertainty in determining the eigenfrequency values from the data, and the corresponding density uncertainty. The location of the plasmapause is shown to reside between $L = 3.09$ and $L = 4.54$, across which the resonance frequency rises with increasing L-shell, and the density drops from ∼800 amu/cc to ∼25 amu/cc. This region has limited coverage, and is part of the CARISMA expansion region. The new CARISMA expansion sites will provide improved spatial resolution along eigenfrequency and density profiles in the plasmapause region.

Through comparison to partner in-situ measurements of the electron density, such as from THEMIS spacecraft potential, the dynamical variations of heavy ion populations may also be determined (e.g. Fraser et al. 2005; Dent et al. 2006). Recent studies have shown that the "archetypal" plasmapause is rarely observed, and structure at the edge of the plasmasphere is created by competition between dynamical erosion and L-dependent refilling (e.g. Dent et al. 2003, 2006). Moreover, care needs to be taken in defining "the" plasmapause location, since different ion species, and electrons, can all indicate sharp gradients at different locations. A very steep plasmapause can create a local, and MLT (and likely time) limited feature of a reversed cross-phase peak (Kale et al. 2007). This corresponds to a local turning point in the Alfven continuum due to the rapid L-variation in density at the sharp plasmapause (Kale et al. 2007). At times, these "negative cross-phase peaks" demonstrate complex structure as a function of frequency, with both positive and negative peaks observed at different frequencies at the same time. Further work is required in order to establish the explanations for these cross-phase features.

Future ground-THEMIS satellite correlative studies can be used to examine the processes leading to dynamical structure of the plasmasphere, and which lead to plasmaspheric refilling. Work is certainly needed to establish whether the negative cross-phase peak results observed by Kale et al. (2007) apply universally to "steep plasmapause" profiles. Given the importance of the plasmasphere and plumes for radiation belt dynamics, THEMIS-CARISMA conjunctions also offer the basis for studies of the role of plasmaspheric drainage plumes in inner magnetosphere wave-particle interactions. Given that the IMAGE satellite is no longer operational following its failure in late 2005, ground-based magnetometers may offer a unique method for monitoring plume dynamics (e.g. Kale et al. 2008, in preparation). Ion outflow data from low Earth orbit, such as from the Canadian enhanced Polar Outflow Probe (e-POP) satellite (e.g. Yau et al. 2006) where spacecraft charging is less of a problem, can also be used to inform refilling studies. Additionally GPS TEC available from the Canadian High Arctic Ionospheric Network (CHAIN) and from the CHAIN GPS receiver deployed at the MSTK CARISMA station may also be employed in order to examine the ionospheric density variations associated with plasmaspheric depletion, refilling and dynamical plumes.

7 Conclusions

In this review, we have outlined some of the capabilities of the expanded CARISMA array for completing solar–terrestrial science. As part of the CSA funded Canadian Geospace Monitoring (CGSM) ground-based network, CARISMA data from an expanded array of fluxgate magnetometers and new induction coil magnetometers provides a powerful infrastructure to address scientific questions at the forefront of international efforts. With new

real-time satellite data collection infrastructure, local data loggers, and increased cadence the collective array enables the high resolution characterization of magnetic activity on a continent scale. This magnetic activity results from waves and currents driven in the magnetosphere by solar forcing, providing a magnetic window on the solar–terrestrial interaction. CARISMA magnetometers are the only Canadian instrumentation which provides data to the formal THEMIS dataset. When combined with in-situ data from the THEMIS probes, which are regularly magnetically conjugate to the CARISMA array, the collective ground-satellite data set represents a powerful tool which can be used to address all three of the THEMIS mission's scientific objectives.

References

W. Allan et al., Geophys. Res. Lett. **23**(7), 765 (1996)
W. Allan, S.P. White, E.M. Poulter, Planet. Space. Sci. **34**(4), 371 (1986)
B.J. Anderson, M.J. Engebretson, J. Geophys. Res. **100**(A6), 9591 (1995)
B.J. Anderson et al., J. Geophys. Res. **95**(A7), 10495 (1990)
B.J. Anderson et al., J. Geophys. Res. **107**(A6), 1079 (2002)
V. Angelopoulos, Space Sci. Rev. (2008). doi:10.1007/s11214-008-9336-1
T. Araki, in *Solar Wind Sources of Ultra Low Frequency Wave Pulsations*, ed. by M. Engebretson, K.T. Takahashi, M. Scholer (Am. Geophys. Union, Washington, 1994), p. 183
R.L. Arnoldy et al., J. Geophys. Res. **103**, 23581 (1998)
H.U. Auster et al., Space Sci. Rev. (2008). doi:10.1007/s11214-008-9365-9
L.J. Baddeley et al., Ann. Geophys. **22**, 4229 (2004)
D.N. Baker et al., Nature (2004). doi:10.1038/nature03116
L.N. Baransky et al., Planet. Space Sci. **38**(12), 1573 (1985)
W. Baumjohann, K.-H. Glassmeier, Planet. Space Sci. **32**(11), 1361 (1984)
P.P. Belyaev et al., J. Atmos. Terr. Phys. **52**(9), 781 (1990)
J. Bortnik et al., J. Geophys. Res. **113**, A04201 (2008). doi:10.1029/2007JA012867
J. Boskova et al., J. Atmos. Terr. Phys. **55**(11–12), 1595 (1993)
D.H. Brautigam, J.M. Albert, J. Geophys. Res. **105**(A1), 291 (2000)
A.J. Brizard, A.A. Chan, Phys. Plasmas **6**(12), 4548 (1999)
A.J. Brizard, A.A. Chan, Phys. Plasmas **8**(11), 4762 (2001)
A.J. Brizard, A.A. Chan, Phys. Plasmas (2004). doi:10.1063/1.1773554
M. Cao et al., J. Geophys. Res. **99**(A5), 8731 (1994)
D.L. Carpenter, J. Geophys. Res. **68**, 1675 (1963)
L. Chen, A. Hasegawa, J. Geophys. Res. **96**(A2), 1503 (1991)
Y. Chen et al., J. Geophys. Res. (2007). doi:10.1029/2007JA012314
G. Chisham et al., Planet. Space Sci. **40**(7), 953 (1992)
G. Chisham et al., J. Geophys. Res. **102**(A5), 9619 (1997)
G. Chisham, I.R. Mann, J. Geophys. Res. **104**(A7), 14717 (1999)
M. Cramoysan et al., Ann. Geophys. **13**, 583 (1995)
A.W. Degeling et al., Planet. Space Sci. (2007). doi:10.1016/j.pss.2006.04.039
Z.C. Dent et al., Geophys. Res. Lett. (2003). doi:10.1029/2003GL0169146
Z.C. Dent et al., J. Geophys. Res. (2006). doi:10.1029/2005JA011046
S.R. Elkington et al., J. Atmos. Sol. Terr. Phys. **64**(5–6), 607 (2002)
S.R. Elkington et al., J. Geophys. Res. (2003). doi:10.1029/2001JA009202
M.J. Engebretson et al., J. Geophys. Res. (2002). doi:10.1029/2001JA000198
M.J. Engebretson et al., J. Geophys. Res. 113, (2008). doi:10.1029/2007JA012362
D.H. Fairfield et al., J. Geophys. Res. (2007). doi:10.1029/2006JA012052

C.G. Fälthammer, J. Geophys. Res. **71**(5), 1487 (1966)

J.E. Foat et al., Geophys. Res. Lett. **25**(22), 4109 (1998)

B.J. Fraser, J. Atmos. Terr. Phys. **38**, 1141 (1976)

B.J. Fraser et al., Geophys. Res. Lett. (2005). doi:10.1029/2004/GL21315

R.H. Friedel et al., J. Atmos. Sol. Terr. Phys. **64**(2), 265 (2002)

K.-H. Glassmeier, Ann. Geophys. **10**(547), 547 (1992)

K.-H. Glassmeier, M. Stellmacher, J. Geophys. Res. **105**(18), 847 (2000)

H. Gough, D. Orr, Planet. Space Sci. **32**(5), 619 (1984)

R.A. Greenwald, A.D.M. Walker, Geophys. Res. Lett. **7**, 745 (1980)

H. Hasegawa et al., Nature **430**(7001), 755 (2004)

S.R. Hebden et al., Ann. Geophys. **23**(5), 1711 (2005)

R.B. Horne, R.M. Thorne, J. Geophys. Res. **98**(A6), 9233 (1993)

R.B. Horne, R.M. Thorne, J. Geophys. Res. **99**(A9), 17259 (1994)

R.B. Horne, R.M. Thorne, Geophys. Res. Lett. **25**(15), 3011 (1998)

R.B. Horne et al., J. Geophys. Res. (2005). doi:10.1029/2004JA010811

M.K. Hudson et al., Adv. Space Res. **25**(12), 2327 (2000)

W.J. Hughes et al., Nature **275**(5675), 43 (1978)

W.J. Hughes, in *Solar Wind Sources of Magnetospheric Ultra-Low-Frequency Waves*, ed. by M.J. Engebretson, K. Takahashi, M. Scholer (American Geophysical Union, Washington, 1994), p. 1

J.A. Jacobs et al., J. Geophys. Res. **69**(1), 180 (1964)

J.A. Jacobs, T. Watanabe, J. Atmos. Sol. Terr. Phys. **26**(8), 825–829 (1964)

V.K. Jordanova et al., J. Geophys. Res. **106**(A1), 7 (2001)

Z.C. Kale et al., J. Geophys. Res. **112** (2007). doi:10.1029/2007JA012367

R. Kataoka, H. Fukunishi, L.J. Lanzerotti, J. Geophys Res. **108**, 1436 (2003). doi:10.1029/2003JA010202

L. Kepko, M.G. Kivelson, J. Geophys. Res. **104**(A11), 25021 (1999)

L. Kepko, M.G. Kivelson, K. Yumoto, J. Geophys. Res. **106**(A2), 1903 (2001)

L. Kepko, H.E. Spence, H.J. Singer, Geophys. Res. Lett. (2002). doi:10.1029/2001GL014405

M.G. Kivelson, D.J. Southwood, Geophys. Res. Lett. **12**(1), 49 (1985)

M.G. Kivelson, J. Etcheto, J.G. Trotignon, J. Geophys. Res. **89**(A11), 9851 (1984)

M.G. Kivelson, D.J. Southwood, J. Geophys. Res. **96**(A2), 1661 (1991)

J.U. Kozyra et al., J. Geophys. Res. **89**(A4), 2217–2233 (1984)

J.U. Kozyra et al., in *Geophys. Monogr. Ser.*, vol. 98, ed. by B.T. Tsurutani et al. (AGU, Washington, 1997), p. 187

G. Le, C.T. Russell, J. Geophys. Res. **101**(A2), 2571 (1996)

L.C. Lee, J.V. Olson, Geophys. Res. Lett. **7**, 777 (1980)

M.R. Lessard et al., Geophys. Res. Lett. (2006). doi:10.1029/2006GL026411

M. Lester, W.J. Hughes, H.J. Singer, J. Geophys. Res. **88**(A10), 7958 (1983)

X. Li et al., Geophys. Res. Lett. (2006). doi:10.1029/2006GL026294

T.M. Loto'aniu, B.J. Fraser, C.L. Waters, J. Geophys. Res. (2005). doi:10.1029/2004JA010816

T.M. Loto'aniu et al., J. Geophys. Res. (2006). doi:10.1029/2005JA011355

A.T.Y. Lui et al., J. Geophys. Res. **96**(A7), 11389 (1991)

R.L. Lysak, Feedback instability of the ionospheric resonant cavity. J. Geophys. Res. **96**(A2), 1553–1568 (1991)

R.L. Lysak, in *Auroral Plasma Dynamics*, ed. by R.L. Lysak (American Geophysical Union, Washington, 1994), p. 121

I.R. Mann, A.N. Wright, Geophys. Res. Lett. **26**(16), 2609 (1999)

I.R. Mann, G. Chisham, S. Bale, J. Geophys. Res. **103**(A3), 4657 (1998)

I.R. Mann et al., J. Geophys. Res. **104**(A1), 333 (1999)

I.R. Mann et al., Ann. Geophys. **20**(4), 405 (2002)

I.R. Mann et al., J. Atmos. Sol. Terr. Phys. **66**(2), 187 (2004)

I.R. Mann et al., EOS Transact. AGU, Fall Meet. Suppl. **88**(52), Abstract SM14A-04 (2007)

R.A. Mathie, I.R. Mann, Geophys. Res. Lett. **27**(20), 3261 (2000a)

R.A. Mathie, I.R. Mann, Geophys. Res. Lett. **27**(24), 4017 (2000b)

R.A. Mathie, I.R. Mann, J. Geophys. Res. **105**(A5), 10713 (2000c)

R.A. Mathie, I.R. Mann, J. Geophys. Res. **106**(A12), 29783 (2001)

R.A. Mathie et al., Geophys. Res. Lett. **26**(6), 659 (1999a)

R.A. Mathie et al., J. Geophys. Res. **104**(A4), 7025 (1999b)

J.P. McFadden et al., Space Sci. Rev. (2008, this issue)

J.F. McKenzie, Planet. Space Sci. **18**(1), 1 (1970)

R.L. McPherron et al., J. Geophys. Res. **78**(16), 3131 (1973)

S.B. Mende et al., Geophys. Res. Lett. (2007). doi:10.1029/2007GL030850

S.B. Mende et al., Space Sci. Rev. (2008, this issue)

F.W. Menk et al., J. Geophys. Res. **104**(A9), 19955 (1999)

F.W. Menk et al., J. Geophys. Res. **105**(A4), 7747 (2000)

F.W. Menk et al., J. Geophys. Res. (2004). doi:10.1029/2003JA010097

N.P. Meredith et al., J. Geophys. Res. (2003). doi:10.1029/2002JA009700

N.P. Meredith et al., J. Geophys. Res. (2007). doi:10.1029/2007JA012413

R.H. Millan et al., Geophys. Res. Lett. (2002). doi:10.1029/2002GL015922

D.K. Milling et al., Geophys. Res. Lett. **28**(1), 115 (2001)

D.K. Milling et al., Geophys. Res. Lett. **35**, 0 (2008). doi:10.1029/2008GL033672

A. Miura, J. Geophys. Res. **97**(A7), 10655 (1992)

K.R. Murphy et al., J. Geophys. Res. (2008). doi:10.1029/2008JA013548

D.L. Murr, W.J. Hughes, Geophys. Res. Lett. **30**, 1354 (2003). doi:10.1029/2002GL015498

K. Mursula et al., J. Geophys. Res. **102**(A8), 17611 (1997)

K. Mursula et al., J. Atmos. Sol. Terr. Phys. **62**(4), 299 (2000)

M. Nose et al., Earth Planets Space **50**(9), 773 (1998)

T.P. O'Brien, R.L. McPherron, J. Geophys. Res. (2003). doi:10.1029/2002JA009324

T.P. O'Brien et al., J. Geophys. Res. (2003). doi:10.1029/2002JA009784

T.P. O'Brien, M.B. Moldwin, Geophys. Res. Lett. (2003). doi:10.1029/2002GL016007

T.P. O'Brien et al., J. Geophys. Res. **106**(A8), 15533 (2001)

J.V. Olson, J. Geophys. Res. **104**(A8), 17499 (1999)

L.G. Ozeke, I.R. Mann, J. Geophys. Res. **106**(A8), 15583 (2001)

L.G. Ozeke, I.R. Mann, J. Geophys. Res. (2008). doi:10.1029/2007JA012468

L. Ozeke, I.R. Mann, I.J. Rae, J. Geophys. Res. (2008). doi:10.1029/2008JA013041

A. Parent et al., in *Proceedings of the 8th International Conference on Substorms*, ed. by M. Syrjäsuo, E. Donovan (University of Calgary, Canada, 2007), p. 225

C.G. Park, J. Geophys. Res. **79**(1), 169 (1974)

J.L. Posch et al., J. Atmos. Sol. Terr. Phys. **69**, 1775 (2007). doi:10.1016/j.jastp.2007.07.015

Z.-Y. Pu, M. Kivelson, J. Geophys. Res. **88**(2), 841 (1983)

I.J. Rae et al., J. Geophys. Res. (2005). doi:10.1029/2005JA011007

I.J. Rae et al., Planet. Space Sci. (2007a). doi:10.1016/j.pss.2006.02.009

I.J. Rae et al., Ann. Geophys. **25**(12), 2529 (2007b)

I.J. Rae et al., J. Geophys. Res. (2008a). doi:10.1029/2008JA013559

I.J. Rae et al., J. Geophys. Res. (2008b). doi:10.1029/JA2008JA013771

J. Rauch, A. Roux, J. Geophys. Res. **87**(A10), 8191 (1982)

G.J. Rickard, A.N. Wright, J. Geophys. Res. **100**, 3531 (1995)

G. Rostoker, S.-I. Akasofu, J. Foster, R.A. Greenwald, Y. Kamide, K. Kawasaki, A.T.Y. Lui, R.L. McPherron, C.T. Russell, Magnetospheric substorms—definition and signatures. J. Geophys. Res. **85**(A4), 1663–1668 (1980)

G. Rostoker, B.T. Sullivan, Planet. Space Sci. **35**, 429 (1987)

G. Rostoker et al., Space Sci. Rev. **71**(1–4), 743 (1995)

G. Rostoker, S. Skone, D.N. Baker, Geophys. Res. Lett. **25**(19), 3701 (1998)

J.M. Ruohoniemi et al., J. Geophys. Res. **96**(A9), 15697 (1991)

T. Saito, Sci. Rep. Tohoku Univ., 5, Geophys. **13** 53 (1961)

J.C. Samson, J.A. Jacobs, G. Rostoker, J. Geophys. Res. **76**(16), 3675 (1971)

J.C. Samson et al., Geophys. Res. Lett. **19**(5), 441 (1992)

M. Schulz, L.J. Lanzerotti, *Particle Diffusion in the Radiation Belts* (Springer, New York, 1974)

Y.Y. Shprits et al., Geophys. Res. Lett. (2004). doi:10.1029/2004GL019591

Y.Y. Shprits et al., Ann. Geophys. **23**(4), 1467 (2005)

Y.Y. Shprits et al., Geophys. Res. Lett. (2006). doi:10.1029/2005GL024256

D.G. Sibeck, V. Angelopoulos, THEMIS science objectives and mission phases. Space Sci. Rev. (2008). doi:10.1007/s11214-008-9393-5

D.G. Sibeck et al., J. Geophys. Res. (1999). doi:10.1029/1998JA900021

A.J. Smith et al., J. Geophys. Res. **104**(A5), 12351 (1999)

D.J. Southwood, J. Geophys. Res. **81**(19), 3340 (1976)

D.J. Southwood, J.W. Dungey, R.J. Etherington, Planet. Space Sci. 17 (1969)

D.J. Southwood, M.G. Kivelson, J. Geophys. Res. **87**(NA3), 1707 (1982)

M. Spasojević et al., Geophys. Res. Lett. (2004). doi:10.1029/2003GL018389

D. Summers, R.M. Thorne, J. Geophys. Res. (2003). doi:10.1029/2002JA009489

T. Takeuchi et al., J. Geophys. Res. **105**(A8), 18835 (2000)

L.V. Tverskaya et al., Geomagn. Aeron. **26**(5), 864 (1986)

M. Usanova et al., Geophys. Res. Lett. (2008). doi:10.1029/2008GL034458

G. Vetoulis, L. Chen, J. Geophys. Res. **21**(19), 2091 (1994)
A.D.M. Walker, J. Atmos. Sol. Terr. Phys. **62**(9), 799 (2000)
A.D.M. Walker et al., J. Geophys. Res. **97**(A8), 12187 (1992)
C.L. Waters, F.W. Menk, B.J. Fraser, Geophys. Res. Lett. **18**(12), 2293 (1991)
C.L. Waters, J.C. Samson, E.F. Donovan, J. Geophys. Res. **100**(A5), 7987 (1995)
C.L. Waters et al., J. Geophys. Res. **107**, 1284 (2002). doi:10.1029/2001JA000224
C.E.J. Watt et al., J. Geophys. Res. (2005). doi:10.1029/2004JA010877
M.E. Wilson et al., Ann. Geophys. **24**, 3027 (2006)
A.N. Wright, J. Geophys. Res. **99**(A1), 159 (1994)
A.N. Wright, G.J. Rickard, J. Geophys. Res. **100**(A12), 23703 (1995)
A.N. Wright, I.R. Mann, in *Magnetospheric ULF Waves: Synthesis and New Directions*, ed. by K. Takahashi et al.. AGU Monograph Series, vol. 169 (Am. Geophys. Union, Washington, 2006)
A.G. Yahnin et al., Ann. Geophys. **21**(3), 779 (2003)
A.W. Yau, H.G. James, W. Liu, Adv. Space Res. (2006). doi:10.1016/j.asr.2005.01.058